NASA/TM–2011–215988

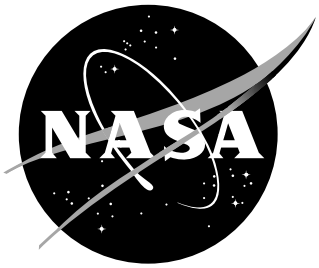

Issues of Long-Term Cryogenic Propellant Storage in Microgravity

C. B. Muratov
Department of Mathematical Sciences, New Jersey Institute of Technology, Newark, NJ 07102

V. V. Osipov, V. N. Smelyanskiy
Applied Physics Group, Intelligent Systems Division
NASA Ames Research Center Moffett Field, CA 94035-1000

October 2011

NASA STI Program . . . in Profile

Since its founding, NASA has been dedicated to the advancement of aeronautics and space science. The NASA scientific and technical information (STI) program plays a key part in helping NASA maintain this important role.

The NASA STI Program operates under the auspices of the Agency Chief Information Officer. It collects, organizes, provides for archiving, and disseminates NASA's STI. The NASA STI Program provides access to the NASA Aeronautics and Space Database and its public interface, the NASA Technical Report Server, thus providing one of the largest collection of aeronautical and space science STI in the world. Results are published in both non-NASA channels and by NASA in the NASA STI Report Series, which includes the following report types:

- TECHNICAL PUBLICATION. Reports of completed research or a major significant phase of research that present the results of NASA programs and include extensive data or theoretical analysis. Includes compilations of significant scientific and technical data and information deemed to be of continuing reference value. NASA counterpart of peer-reviewed formal professional papers, but having less stringent limitations on manuscript length and extent of graphic presentations.
- TECHNICAL MEMORANDUM. Scientific and technical findings that are preliminary or of specialized interest, e.g., quick release reports, working papers, and bibliographies that contain minimal annotation. Does not contain extensive analysis.
- CONTRACTOR REPORT. Scientific and technical findings by NASA-sponsored contractors and grantees.
- CONFERENCE PUBLICATION. Collected papers from scientific and technical conferences, symposia, seminars, or other meetings sponsored or co-sponsored by NASA.
- SPECIAL PUBLICATION. Scientific, technical, or historical information from NASA programs, projects, and missions, often concerned with subjects having substantial public interest.
- TECHNICAL TRANSLATION. English-language translations of foreign scientific and technical material pertinent to NASA's mission.

Specialized services also include creating custom thesauri, building customized databases, and organizing and publishing research results.

For more information about the NASA STI Program, see the following:

- Access the NASA STI program home page at ***http://www.sti.nasa.gov***
- E-mail your question via the Internet to help@sti.nasa.gov
- Fax your question to the NASA STI Help Desk at 443-757-5803
- Phone the NASA STI Help Desk at 443-757-5802
- Write to:
  NASA STI Help Desk
  NASA Center for AeroSpace Information
  7115 Standard Drive
  Hanover, MD 21076–1320

NASA/TM–2011–215988

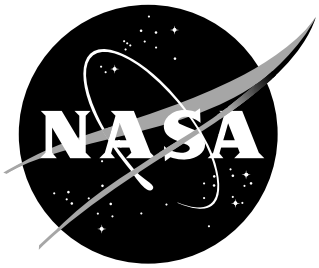

Issues of Long-Term Cryogenic Propellant Storage in Microgravity

C. B. Muratov
Department of Mathematical Sciences, New Jersey Institute of Technology, Newark, NJ 07102

V. V. Osipov, V. N. Smelyanskiy
Applied Physics Group, Intelligent Systems Division
NASA Ames Research Center Moffett Field, CA 94035-1000

National Aeronautics and
Space Administration

NASA Ames Research Center Moffett Field, CA 94035-1000

October 2011

Available from:

NASA Center for AeroSpace Information
7115 Standard Drive
Hanover, MD 21076-1320
443-757-5802

Abstract

Modern multi-layer insulation (MLI) allows to sharply reduce the heat leak into cryogenic propellant storage tanks through the tank surface and, as a consequence, significantly extend the storage duration. In this situation the MLI penetrations, such as support struts, feed lines, etc., become one of the most significant challenges of the tank's heat management. This problem is especially acute for liquid hydrogen (LH2) storage, since currently no efficient cryocoolers exist that operate at very low LH2 temperatures ($\sim$20K). Even small heat leaks under microgravity conditions and over the period of many months give rise to a complex slowly-developing, large-scale spatiotemporal physical phenomena in a multi-phase liquid-vapor mixture. These phenomena are not well-understood nor can be easily controlled. They can be of a potentially hazardous nature for long-term on-orbital cryogenic storage, propellant loading, tank chilldown, engine restart, and other in-space cryogenic fluid management operations. To support the engineering design solutions that would mitigate these effects a detailed physics-based analysis of heat transfer, vapor bubble formation, growth, motion, coalescence and collapse is required in the presence of stirring jets of different configurations and passive cooling devices such as MLI, thermodynamic vent system, and vapor-cooled shield. To develop physics-based models and correlations reliable for microgravity conditions and long-time scales there is a need for new fundamental data to be collected from on-orbit cryogenic storage experiments. Our report discusses some of these physical phenomena and the design requirements and future studies necessary for their mitigation. Special attention is payed to the phenomena occurring near MLI penetrations.

Contents

1 Introduction

This paper aims at discussing some of the basic physics issues associated with long-term storage of cryogenic liquids in zero gravity or microgravity environments. By "long-term" we mean, for example, the durations of the currently envisioned extended storage periods in the low earth orbit (LEO), which range from months to years. For NASA's present and future space exploration missions, understanding the behavior of cryogenic liquids over long periods of storage is of crucial importance, because of the fundamental role played by cryogenic propellants, primarily liquid hydrogen (LH2) and liquid oxygen (LOX), in rocket propulsion, specifically for long-range missions [1]. The very feasibility of using liquid propellant engines based on LH2 and LOX in the future long-range missions depends on the success of storing these propellants under microgravity or zero gravity for extended periods of time. One of the currently considered exploration strategies calls for the development of propellant storage and transfer facilities in LEO [2]. These "fuel depots" will need to be able to spend significant amounts of time (at least on the order of several months) in LEO without any substantial propellant losses due to boil-off [2–5]. With the current passive heat insulation technologies, it is theoretically possible to reduce the cryogen boil-off rate to below 3% per month [6]. Even so, this issue becomes a challenge when the required storage duration exceeds 6 months, and yet a greater one for manned missions to Mars [7].

Cryogenic fluid management (CFM) in microgravity provides a number of fundamental physical challenges, many of which were previously discussed in the literature [6, 8–13]. This is especially relevant to storage of LH2 because of its low critical temperature. One of the main features of

microgravity environments is that due to much-reduced levels of g-forces and their generally time-varying character, the vapor bubbles that form as a result of boil-off at the tank walls mainly near MLI penetrations (hot-spots) will not rise quickly towards the ullage space, as they do under normal gravity. Instead, they may slowly grow to very large sizes (tens of centimeters), or they may detach from the wall, migrate toward the stagnation areas of the stirring flow and accumulate there, forming regions of saturated liquid and complicated foam-like vapor-liquid structures whose properties may be not easy to control. These processes are governed by the complex heat transfer mechanisms in the near-wall region; capillary and g-forces; complex dynamics of nucleate boiling; bubble growth, detachment and collapse; chemical traces that can accumulate in the liquid with time and affect its properties. In long-term storage missions foam or bubble colonies can grow at the expense of the single ullage space. They may not be easily removed by tank pressurization because the heat released from vapor condensation may raise the temperature of the liquid surrounding the bubbles to the saturation temperature at the higher pressure. Capillary forces may be sufficiently strong to prevent the detachment of the foam from the tank walls by any realistic stirring flow that keeps the ullage intact. Basic challenges, therefore, include control of the tank pressure, temperature, ullage space size and location, boil-off venting, and work of liquid acquisition devices (LAD) that can be clogged by the foam. Similarly, since the role of buoyancy-driven convection, which is the main mechanism of heat transfer on earth, is greatly reduced in microgravity, heat transfer mechanisms will be significantly altered. Vapor and fluid motion, in turn, will be dominated by the capillary forces, heat transfer-mediated bubble dynamics, bubble coalescence, Ostwald ripening and the induced thermocapillary convection. The resulting bubble patterns and near-wall dynamics, especially around the MLI penetrations can substantially depend on the type of the wall material, chemical traces, vibrations and other external factors.

In view of these complications, the basic technical issues that need to be dealt with in today's design of successful cryogenic storage and transfer devices for long-term operation in microgravity: heat transfer management, pressure control, design of tank stirring, mass gauging, liquid acquisition, and fluid transfer are much more challenging [11], compared to the Apollo era short duration missions, in which a low level of gravity was propulsively maintained [14–16].

A successful treatment of the pressing technical issues of cryogen management in microgravity is impossible without a thorough mechanistic understanding of the underlying physical processes of nucleate boiling. Surprisingly, detailed physical understanding of nucleate boiling phenomena is still lacking today (see e.g. [17]). This may be due to the fact that boiling is a strongly non-equilibrium phenomenon in which an interplay between stochastic nucleation events at the micro-scale and complicated deterministic nonlinear dynamics at macro-scale takes place (for reviews, see [18–21]). At the same time, in view of the fact that microgravity presents quite a different environment compared to the usual environment on earth, one should exercise caution in applying the engineering correlations developed under earth gravity conditions to the design of cryogenic systems to be operated in space [21, 22]. To address the above technology gaps, it is necessary to collect fundamental data on liquid-vapor structure and dynamics during long-term storage in microgravity from carefully designed in-space long-duration experiments. Experimental work should be done in combination with a detailed physics analysis, mechanistic modeling, first principles computational and multi-scale approaches.

Here we perform some basic physical estimates in order to evaluate the relative importance of different physical processes during long-term cryogenic storage. We concentrate our efforts on LH2, since it is the cryogen of primary importance to rocket propulsion and is also the most difficult

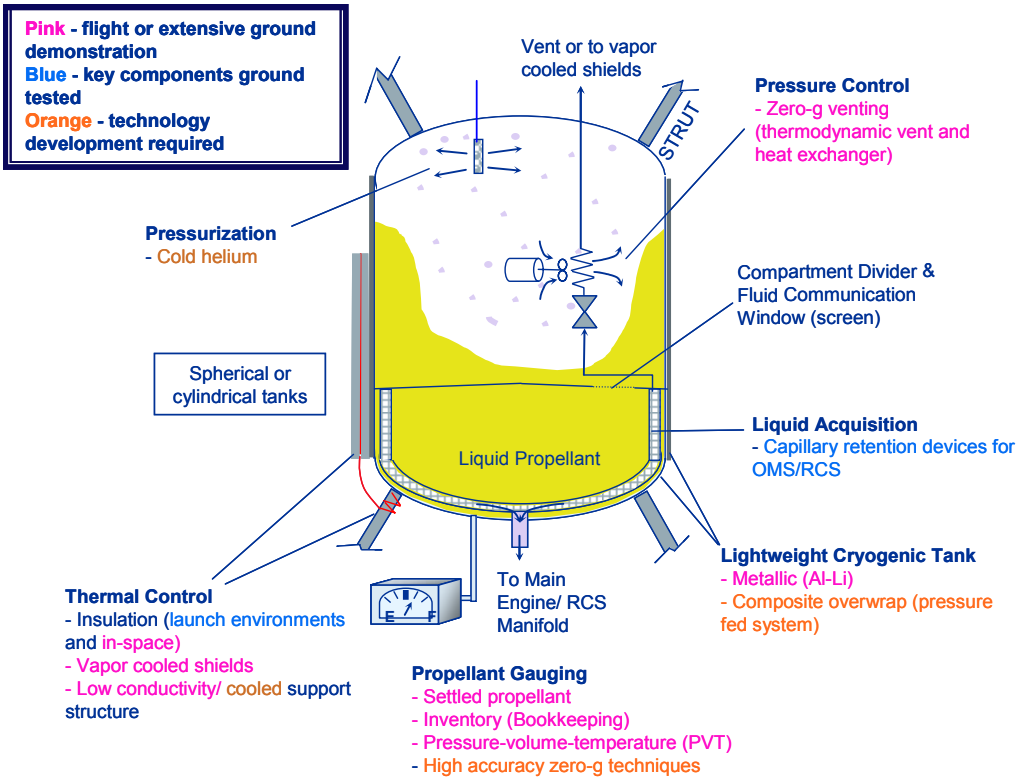

Figure 1. The schematics of a cryogenic storage tank (from [6]).

in terms of CFM due to its low boiling point. Let us emphasize that we aim at obtaining only relatively rough estimates that take into account the *long-term* nature of storage. Thus, our main tool will be dimensional analysis, with minimal reference to more advanced mathematical tools. Once the main physical processes acting on the considered long timescales are identified, relevant space experiments can be designed and more precise calculations may be made using advanced mathematical and high-fidelity computational tools. In short, our main goal is to identify these processes and the issues, such as safety hazards and design optimization parameters, which arise specifically during extended periods in microgravity.

2 Background

We start with some basic considerations relevant to large-scale cryogenic storage in microgravity. A conceptual representation of a cryogenic fuel tank [6] is shown in Fig. 1. To fix ideas, let us consider one of the proposed designs for the LH2 tank of the Earth Departure Stage (EDS) for moon missions [23], in which the tank has the shape of a rounded cylinder with height $H_0 = 12$ m and radius $R_0 = 2.5$ m, containing 15 tons of LH2. The scale of the tank is similar to that used in

the S-IVB stage of the Saturn V rocket in the 1960's and 70's, and a brief comparison is, therefore, appropriate.

Indeed, NASA's most comprehensive experience with large-scale cryogenic storage tanks in orbital conditions goes back to the Apollo moon missions[1] [15, 16, 25] (see also reviews of other CFM experimental activities in [9, 14]). The third stage of the Saturn V rocket was propelled by LH2 and LOX, containing 19,800 kg and 88,800 kg, respectively (here and below the numbers are from the Apollo 17 mission [26, 27]). About a quarter of the propellants (5,000 kg of LH2 and 25,200 kg of LOX) was utilized for orbital insertion, and the remaining amount was used for the translunar injection burn. Once in orbit, the third stage spent about 3 hours in LEO. The tank insulation employed (polyurethane foam attached to the interior side of the tank wall) brought the LH2 boil-off amount down to about 1,000 kg, still an acceptable margin of under 10% of LH2 available for the second burn. The flow of continuously vented hydrogen vapor (GH2) was used to provide enough thrust (on the order of $10^{-5}g - 10^{-4}g$) to ensure that the propellants were settled at the bottoms of the tanks at all times during the orbital coast phase. The presence of small upward g-force ensured that the boil-off bubbles rose in the thin convective layer along the tank walls without entering the bulk liquid. Immediately prior to the second burn, the LH2 tank was rapidly pressurized by the stored heated helium gas (GHe), raising the tank pressure from about 1.5 to 2 atm. This short-time pressurization, followed by firing of the ullage motors must have condensed the smaller vapor bubbles and made the larger bubbles move towards the ullage. The resulting LH2 liquid at the bottom of the tank should have, therefore, contained little or no bubbles, allowing to safely fire the engine. After that, the thrust of the engine would maintain the gas-free liquid at the LH2 intake, with screens adding an extra protection.

While hugely successful in bringing man to the surface of the moon and back, this approach may not be applied to the missions currently under consideration. They key reason why the Apollo CFM approach worked for the lunar program was that the required in-orbit storage time for the cryogenic propellants was short enough, so it was possible to tolerate a large boil-off rate and, as a consequence, avoid microgravity conditions altogether during the time in orbit. Thus, the Apollo approach carefully avoided dealing with long-term CFM issues associated with microgravity. Any kind of large modern long-range mission, however, would require storing cryogens for extended periods of time. To achieve this, one would need to drastically reduce the amount of boil-off and work in micro-g or zero-g environments. New approaches are, therefore, needed to answer these emerging challenges.

Modern multi-layer insulation (MLI) allows to dramatically reduce the boil-off rate compared to the Apollo missions. Let us assume that the tank is wrapped in an MLI blanket of 50 layers. Using the Lockheed correlation [28], we can estimate the heat flux through the MLI, given the outer environment temperature $T_0 \simeq 240$K, to be $q_0 \simeq 7.4 \times 10^{-2}$ W/m^2 [29]. Taking for simplicity the tank area to be $S_0 = 2\pi R_0 H_0 \simeq 200\text{m}^2$, we obtain a lower bound of $Q_0 = q_0 S_0 \simeq 15$ W for the total heat flow into the tank, with the corresponding boil-off rate of at least 90 kg/month, or 0.6% of the propellant mass per month. Of course, these numbers must underestimate the actual heat flow, since they do not take into account heat leaks through various MLI penetrations by struts, feed lines, etc., as well as imperfections in the MLI itself. Let us also note that the heat flux depends

[1] We note that liquid helium (LHe) has flown for extended periods of time on a number of scientific missions [13]. Let us point out, however, that in these missions LHe is chilled down to the superfluid state. This makes the case of LHe storage very different from all other cryogens, since, in contrast to all other cryogens, superfluid LHe has infinite heat conductivity [24], which prevents it from thermal stratification and nucleate boiling.

very sensitively on the outer environment temperature T_0. In the extreme case of $T_0 \simeq 400$K, we find $q_0 \simeq 0.8$ W/m^2, an order of magnitude higher than the one computed previously, resulting in the heat flow of $Q_0 \simeq 160$ W and an unacceptably high boil-off rate of 6% per month.

Even with very efficient MLI insulation, the loss of propellant becomes prohibitive for extended missions. Therefore, active boil-off reduction techniques are necessary to improve retention of usable propellants. One idea that has been developed over recent years is to employ zero-boil-off technology (ZBOT) [3, 30–32]. While ZBOT approach was demonstrated to be successful in the case of cryogens with higher boiling points, e.g. LOX, no cryocoolers enabling ZBOT yet exist that could operate at LH2 temperatures [33]. Another idea to further decrease the heat inflow into the LH2 tank is to use the concept of broad area cooling (BAC), whereby the tank is surrounded by a network of tubes carrying a coolant fluid [6, 12, 31, 33, 34]. Circulating the fluid through the tubes with the subsequent heat removal by cryocoolers operating at higher temperature may then allow to significantly reduce heat penetration. Use of vapor-cooled shield (VCS) [6, 7, 13, 35] would be particularly efficient, since thermalizing GH2 with the outer layers of the MLI could increase the storage time up to a factor of 6 (see Secs. 3.1.4 and 3.1.5 for more details). We note, however, that strong localized heat leaks through MLI penetrations (the main subject of the present paper) provide one of the greatest CFM challenges for long-term cryogenic storage.

3 Physics of long-term cryogenic storage

Let us now perform some basic estimates for the sample 15-ton LH2 tank whose dimensions were introduced in Sec. 2. Since the precise parameters of the MLI performance admit significant variation, we will take an overall heat leak per unit area with an ample margin: $q_0 = 0.4$ W/m^2, giving a total heat influx of 80W through the MLI (see also [6,29]). In addition, we will assume that another 40W of heat enters the tank via penetrations in the form of localized heat sources, giving the total incoming heat flow of $Q_0 = 120$W. We note that MLI penetrations, such as support struts, feed lines, etc., may provide the greatest challenge in the tank's heat management. For example, taking the characteristic parameters of the orbiter support strut from the Space Shuttle external tank, which is a tubular structure of radius $R \simeq 20$ cm, thickness $d \simeq 5$ mm and length $L \simeq 1$ m, with thermal conductivity $\kappa \simeq 7$ W/(m·K) of Inconel 718 alloy at $T \simeq 100$K [36], we find that the conductive heat leak into the tank can be estimated as $Q_{\rm strut} \simeq 2\pi\kappa R d T_0/L = 11$W. Note that this formula may significantly underestimate $Q_{\rm strut}$, since it does not take into account the additional heat entering the strut through its own thermal insulation. Similarly, for a titanium strut with $d \simeq 1$ cm and $\kappa \simeq 15$ W/(m·K) [37] we find $Q_{\rm strut} \simeq 45$W, and for Al 2219 strut with $d \simeq 1.5$ cm and $\kappa \simeq 70$ W/(m·K) [38] we find a prohibitively high $Q_{\rm strut} \simeq 320$W. In view of the preceding considerations, however, the conductive heat leaks must not exceed several Watts per penetration in order for the tank to remain within the acceptable thermal budget. There is, therefore, a significant trade-off between the structural and thermal properties of the materials used, requiring strong materials with low thermal conductivity and a possible need for external penetration cooling [6].

To proceed, we need to specify the operating parameters for LH2 in the tank. We will assume that the tank is initially at pressure $p_0 = 1.6$ atm, corresponding to the saturation temperature $T_{s0} = 22$K of LH2 (parahydrogen), and that LH2 is subcooled to $T_{L0} = 20.3$K, corresponding to saturation temperature at 1 atm. Here and everywhere below the definitions and values of the parameters of hydrogen used are are listed in Table 1 (for pressure p_0 at saturation [39]).

Table 1. Physical parameters used in the estimates.

Parameter	Value	Meaning
D_{He}	5×10^{-9} m^2/s	Diffusivity of helium in LH2
H_0	12 m	Tank height
P	5 - 15 W	Local heat leak power
Q_0	120 W	Total heat leak
R_0	2.5 m	Tank radius
R_{g0}	1.8 m	Ullage bubble radius
R_{H2}	4,124 J/(kg·K)	Gas constant of hydrogen
R_{He}	2,077 J/(kg·K)	Gas constant of helium
S_0	200 m^2	Tank surface area
T_0	240K	Exterior environment temperature
T_{L0}	20.3K	Subcooling temperature
T_{s0}	22K	Saturation temperature of LH2
V_0	240 m^3	Tank volume
V_{g0}	24 m^3	Ullage volume
c_L	10,820 J/(kg·K)	Specific heat of LH2 at constant pressure
c_w	10 J/(kg·K)	Specific heat of aluminum
g_0	9.81 m/s^2	Earth's acceleration of gravity
g	$0 - 10^{-6} g_0$	Microgravity acceleration
h	1 cm	Tank wall thickness
p_0	1.6 atm	Operating pressure
q_0	0.4 W/m^2	Heat flux through the MLI
q_L	4.35×10^5 J/(kg·K)	Latent heat of LH2 vaporization
β_L	0.0192 K^{-1}	Thermal expansion coefficient of LH2
κ_L	0.101 W/(m·K)	Heat conductance of LH2
κ_v	0.019 W/(m·K)	Heat conductance of GH2
κ_w	20 – 200 W/(m·K)	Heat conductance of aluminum
μ_L	1.16×10^{-5} Pa·s	Viscosity of LH2
ρ_L	68.7 kg/m^3	Density of LH2
ρ_v	2.07 kg/m^3	Density of GH2
ρ_w	2,700 kg/m^3	Density of aluminum
σ_L	1.65×10^{-3} N/m	Surface tension of LH2

Initially, a 10% by volume ullage space with volume $V_{g0} = 24$ m^3 is present, pressurized by cold GHe. The required mass of GHe to produce the excess pressure of 0.6 atm is equal to $M_{He} = (p_0 - p_{\rm atm})V_{g0}/R_{He}T_{L0} \simeq 35$ kg. We note that at large ullage volumes (as LH2 is lost due to boil-off or transfer from the tank), large amounts of cold helium gas are required to pressurize the tank. For example, when the ullage occupies 50% of the tank volume, one would need to supply 175 kg of GHe, respectively. In practice, even greater amounts of helium may be required due to dissolution of GHe in LH2 on long storage timescales (see Sec. 3.1.6). The liquid is subcooled in order to avoid the presence of vapor bubbles in the bulk LH2, which are a potential hazard for engine restart, etc.

Let us briefly comment here on the nature of microgravity environment experienced by the cryogenic tank in LEO. For simplicity, we will consider the tank whose axis is oriented along its velocity vector in a circular orbit. The contributions to g-forces can be separated into three parts. The first part has to do with the spatial non-uniformity of the earth's gravitational field and the centrifugal force. The resulting effective g-force will be a linear function of the distance to earth, vanishing at the tank axial mid-plane. The apparent gravity $\mathbf{g}$ will point away from earth on the side of the tank farthermost from earth, and towards the earth at the side closest to earth. The maximum value of $|\mathbf{g}|$ can be shown to be given by $|\mathbf{g}| \simeq 3g_0 R_0/R_{\rm orbit} \simeq 10^{-6} g_0$, where g_0 is the acceleration of gravity on earth. This gives the Bond number ${\rm Bo} = \rho_L |\mathbf{g}| R_0^2/\sigma_L \simeq 2.5$, indicating that capillary forces balance the apparent gravity forces in the case of the single ullage space. In this situation the equilibrium ullage shape should be approximately an oblate spheroid, whose center is located in the plane passing through the tank's axis and is normal to the direction towards Earth. Note that more generally the apparent g-forces will be time-dependent on the time scale of the orbital period. From the balance of inertia and capillary forces, we find that the characteristic timescale for the ullage to settle is of the order of $t_{\rm ullage} \sim \sqrt{\rho_L R_0^3/\sigma_L} \simeq 15$ mins.

The second contribution to the g-forces is the g-jitter, caused by the motion of the astronauts. These are impulses of acceleration with amplitude roughly of order $10^{-4} g_0$ and duration 1 s in random directions (see e.g. the discussion in [40]). It provides the random vibrational background to the motion of fluid. Note that this contribution would be absent in an unmanned vehicle, or would be the only significant g-force on space missions beyond LEO. Also, both the g-jitter and the space-dependent apparent gravity may assist bubble coalescence. Finally, the third contribution to g-forces is due to the Coriolis force, which arises due to motion of the liquid inside the tank.

3.1 Basic thermodynamics

We begin by evaluating the heat budget of the tank and related issues.

3.1.1 Time to saturation

First, let us calculate the time needed for LH2 to come from the subcooled condition to the saturation temperature under an assumption of perfect mixing (e.g. by an active mixer inside the tank) and in the absence of any boiling and active cooling. This time is given by equating the total amount of heat that entered the tank to the increase in the LH2 heat content:

$$t_{\rm sat,mixed} = \frac{c_L \rho_L (V_0 - V_{g0})(T_{s0} - T_{L0})}{Q_0} \simeq 26 \text{ days}. \tag{1}$$

On the other hand, in the absence of mixing, boiling, and any g-forces the heat will only penetrate from the tank wall to the depth equal to the thermodiffusion length $L = \sqrt{\kappa_L t/(c_L \rho_L)}$ of LH2 in time t. Then the same balance leads to

$$t_{\rm sat,thermodiffusive} = \frac{c_L \rho_L \kappa_L (T_{s0} - T_{L0})^2}{q_0^2} \simeq 16 \text{ days}. \tag{2}$$

Note that, replacing T_{s0} in Eq. (2) with 23K, one can see that in order to achieve a superheat of $\sim$1K at the tank wall (at which nucleate boiling normally occurs in LH2 under normal conditions on earth [41–43]), one would need to wait $t \simeq 40$ days. Finally, for a tank in LEO, taking into account

convective transport in microgravity with $g = 10^{-6} g_0$, we obtain for the tank wall temperature T_w an estimate $T_w - T_{L0} \simeq 0.22$K, which is based on the Nusselt number $\mathrm{Nu}_{R_0} = q_0 R_0/(\kappa_L(T_w - T_{L0})) \simeq 46$ and the Rayleigh number for these parameters $\mathrm{Ra} = g\beta_L(T_w - T_{L0})c_L\rho_L^2 R_0^3/(\mu_L\kappa_L) \simeq 2.8 \times 10^7$, and we used the correlation $\mathrm{Nu}_{R_0} = 0.15\mathrm{Ra}^{1/3}$ [44, Eq. (9.31)]. Thus, the timescale on which the bulk of LH2 heats to the boiling point under the considered heat loads in the absence of any other sources and sinks of heat is about 1 month. Note that on such a long timescale heat conductance alone is sufficient to carry the heat into the tank interior.

3.1.2 Time to complete evaporation

On the other hand, assuming that the tank is maintained at constant pressure p_0, we can find the LH2 storage time by equation the total heat that entered the tank to the heat needed to vaporize all the LH2:

$$t_{\text{storage}} = \frac{(q_L + c_L(T_{s0} - T_{L0}))\rho_L(V_0 - V_{g0})}{Q_0} \simeq 22 \text{ months}. \tag{3}$$

In particular, about 700 kg or ∼5% by volume, of LH2 will be lost to boil-off in one month. This also means that cold GHe needs to be supplied at a rate of ∼16 kg/month to enable maintaining LH2 at subcooled conditions.

3.1.3 Self-pressurization and liquid heating due to mechanical work

While it will take on the order of one month in the absence of any other heat sinks for the bulk of LH2 to be heated to the saturation temperature, local boiling may begin soon due to the localized heat sources through penetrations. With the power from those sources equal to $Q_0 - q_0 S_0 = 40$W and assuming that the boil-off bubbles remain attached to the hot spots on the tank walls, we can estimate the the rate of boil-off of GH2 as

$$\dot{M}_{GH2,\text{boil-off}} = \frac{Q_0 - q_0 S_0}{q_L + c_L(T_{s0} - T_{L0})} \simeq 8 \text{ kg/day}. \tag{4}$$

This results in an increase of the tank pressure at the rate of $\dot{p} = \dot{M}_{GH2,\text{boil-off}} R_{H2} T_{s0}/V_{g0} \simeq 0.3$ atm/day.

Let us also point out that GH2 forming as a result of boil-off performs mechanical work against the liquid in order to expand. The mechanical work done on LH2 will be converted into heat through viscous dissipation in LH2, resulting in a further temperature increase in the liquid bulk. If the boil-off rate $\dot{M}_{GH2,\text{boil-off}}$ is given by Eq. (4), then the work done by the vapor on the liquid is

$$W = \frac{p_0 \dot{M}_{GH2,\text{boil-off}}}{\rho_v} \simeq 7\text{W}. \tag{5}$$

In other words, about 20% of the heat that goes into boil-off ends up heating the bulk liquid. To this, one should also add the amount of work supplied to the liquid through stirring.

3.1.4 Vapor-cooled shield and broad area cooling

The use of VCS can significantly reduce the amount of boil-off by utilizing sensible heat of the boil-off vapor [6, 7, 13, 35]. If the GH2 is simply vented overboard, the amount of heat removed from the tank by the vapor will be $Q_{\text{boil-off}} \simeq q_L \dot{m}_{GH2}$, where $\dot{m}_{GH2}$ is the mass flow of GH2 through the vent. If, on the other hand, the vapor is allowed to thermalize with the outer surface of the MLI at temperature $T_0 \simeq 240$K before being vented, the amount of heat removed equals $Q_{VCS} \simeq (q_L + c_L(T_0 - T_{L0}))\dot{m}_{GH2}$ (taking into account that the specific heat of GH2 does not vary significantly with temperature in the considered interval [39]). The ratio of the two is given by

$$\frac{Q_{VCS}}{Q_{\text{boil-off}}} \simeq 1 + \frac{c_L(T_0 - T_{L0})}{q_L} \simeq 6.5. \tag{6}$$

This means that the use of VCS may reduce boil-off rate for a fixed heat load by over a factor of 6 by intercepting the heat entering into the tank. Further increase in the efficiency may be achieved by passing the warm GH2 through para-ortho converters [7].

Broad area cooling (BAC) is another promising concept that takes advantage of actively cooled GHe running through tubes within the MLI to capture the heat entering from the tank environment and allows to significantly reduce the heat flow per unit area through the MLI [33] (see also [34] for a related concept of active co-storage). One of the main difficulties in applying the BAC technology is efficient thermal bonding of the BAC tubing to the tank structures [6, 31]. Recently, both the "tube-to-tank" and the "tube-to-shield" concepts, whereby the BAC tubing is bonded either directly to the tank wall or to an intermediate layer of the MLI, respectively, have been successfully demonstrated [12, 31, 33, 45]. Let us point out that these concepts may also be used as part of a VCS in conjunction with TVS [35]. Note, however, that in the absence of boiling inside the tank the VCS/TVS system may not be able to intercept the incoming heat, since the heat entering the tank may raise the LH2 temperature locally near the tank walls without producing a pressure or bulk LH2 temperature rise. In this case, the TVS will not operate, and the propellant heating near the tank walls may lead to the potentially dangerous explosive nucleate boiling hazard (see Sec. 3.3.2 for more detail). We also note that in order for the tube-to-tank BAC design to work in an LH2 tank, the cold GHe must be circulated at the temperature of about 20K to avoid boiling of LH2 at the tank walls. Since no efficient cryocoolers currently exist operating at these temperatures, the tube-to-tank concept is not currently applicable to LH2 storage.

3.1.5 Penetration cooling

One of the most challenging problems in the tank heat management is to control the heat leaks from various MLI penetrations, such as the tank structural supports (struts) and propellant feed lines [6]. As was discussed in Sec. 3.1.4, using either VCS or BAC for passive or active cooling of the heat shield, respectively, one could all but eliminate the heat leaks through the MLI into the tank. In this case, the penetrations will provide most of the heat load to the propellant. Note that in contrast to the MLI, where radiative heat transfer dominates, it is not possible to adapt the active tube-to-shield BAC concept operating at intermediate temperatures (see Sec. 3.1.4) to intercept most of the heat coming through penetrations because of the dominant role of conductive heat transfer there. A natural idea (an extension of the VCS concept) is, therefore, to sacrifice some of the stored hydrogen to passively cool the penetrations at their points of contact with the tank walls and, in particular, to suppress possible boiling in those areas. The hydrogen is most

conveniently supplied by TVS, providing a regulatory feedback between the tank heat load and the amount of LH2 used for cooling.

In view of the above discussion, to emphasize the physical phenomena under consideration, in this section we will assume that all heat entering into the tank comes from the penetrations. To make our considerations more quantitative, let us assume for simplicity that the tank contains $N_{\rm strut} = 8$ identical penetration structures (struts). Consistently with our previous assumptions in Sec. 3, each strut is assumed to carry heat in the amount of $Q_{\rm strut} = Q_0/N_{\rm strut} = 15$W conductively into the tank. Under our assumptions about the storage times for the tank, the maximum available LH2 budget (not including the effect of VCS or BAC) that can be used to cool the penetrations is

$$J_{\rm strut} = \frac{Q_{\rm strut}}{q_L} = 3.3 \times 10^{-5}\,{\rm kg/s}. \tag{7}$$

This mass flow of cold GH2 and/or LH2 can be used, e.g., to locally cool the MLI penetrations in the shape of thick pipes. We consider a helical coil in perfect thermal contact with the strut surface, which is formed by winding a thin hydrogen-carrying tube around the strut (see Fig. 2). We now analyse efficiency of such a method of local cooling of the penetrations. In the following, we assume that the cooling tube has characteristic length $L = 10$ m. We also assume that TVS operates in the regime in which LH2 at $p_0 = 1.6$ atm and $T_{L0} = 20.3$K passes through a Joule-Thompson valve with pressure $p_1 = 0.2$ atm at the other end. By considering an isenthalpic process, we then find that hydrogen will be exiting the valve in the form of a two-phase mixture at $T_1 \simeq 16$K containing the mass fraction $\eta \simeq 0.9$ of LH2 [39]. We will consider the situation in which hydrogen from TVS is fully vaporized and is then thermalized with the LH2 propellant before being supplied into the cooling tube (see Fig. 2). In order to estimate the minimum tube radius $R_{\rm tube}$, consider that GH2 is supplied in the form of gas at $T = T_{L0}$. Using the Darcy-Weisbach equation [46, 47]

$$\Delta p = \frac{f \rho u^2 L}{4 R_{\rm tube}} \tag{8}$$

for the pressure drop Δp across the tube, where f is the Darcy friction factor, ρ is the fluid density, u is the average fluid velocity, together with Haaland's approximation to the solution of Colebrook's equation for f [48]:

$$f = \left(1.8 \log_{10} \left[\left(\frac{d_{\rm rough}}{7.4 R_{\rm tube}} \right)^{1.11} + \frac{6.9}{\rm Re} \right] \right)^{-2}, \tag{9}$$

where $d_{\rm rough}$ is the tube surface roughness and Re is the flow Reynolds number, we can estimate the minimum inner tube radius $R_{\rm tube}$ needed to supply the necessary LH2 flow $J_{\rm strut}$ given by Eq. (7). Taking $d_{\rm rough} = 1.5\,\mu$m [44] and $\Delta p = p_1 = 0.2$ atm, we find that the minimum tube radius is $R_{\rm tube} \simeq 1.1$ mm. Note that this estimate is quite insensitive to various assumptions on the parameters, such as the tube roughness or the pressure drop.

Let us now estimate how effective these tubes will be in cooling the penetrations. Assume that the temperature of GH2 flowing inside the coil tube that winds around the hot strut changes from $T_v = T_1$ to $T_v = T_2$. By thermodynamic considerations, we must have

$$Q_{\rm strut} = c_p (T_2 - T_1) J_{\rm strut}. \tag{10}$$

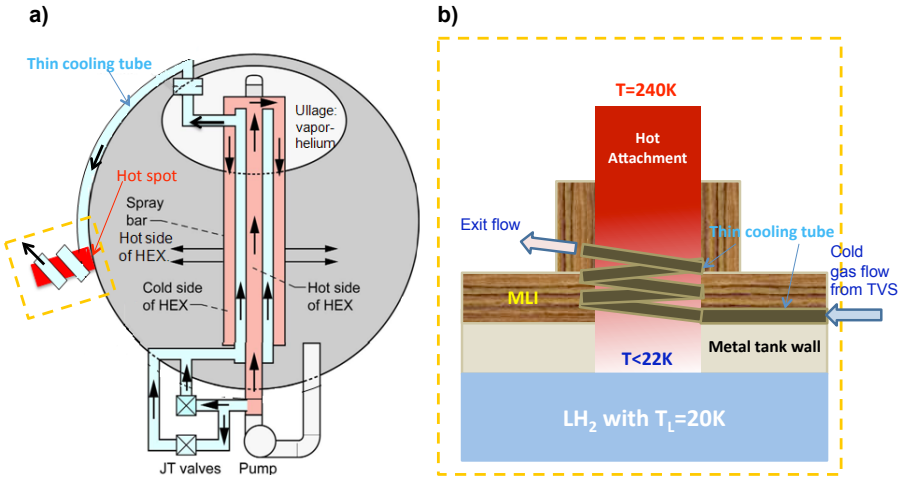

Figure 2. Cooling a penetration by GH2 from TVS. (a) The tank schematics and (b) the close-up of the cooled penetration.

It then follows that the GH2 supplied at $T_1 = T_{L0} = 20.3$K will have the capacity to remove $Q_{\rm strut} = 15$W from the strut, if it is heated to $T_2 \simeq 65$K. Let us now estimate length of the tube which can remove this heat flow. For steady turbulent flow, the heat transfer coefficient $h_{\rm tube}$ can be obtained from the Dittus-Boelter correlation [44]

$$h_{\rm tube} = \frac{\kappa_v}{2R_{\rm tube}}{\rm Nu}_{\rm tube}, \qquad {\rm Nu}_{\rm tube} \simeq 0.023 \times {\rm Re}_{\rm tube}^{4/5}\,{\rm Pr}_{\rm tube}^{1/3}, \tag{11}$$

where ${\rm Nu}_{\rm tube}$, ${\rm Re}_{\rm tube}$ and ${\rm Pr}_{\rm tube}$ are the Nusselt, Reynolds and the Prandtl number associated with the gas flow in the tube, respectively. Note that the formula in Eq. (11) can be equivalently rewritten as

$$h_{\rm tube} = 0.023 c_p \left(\frac{J_{\rm strut}}{\pi R_{\rm tube}^2}\right)^{4/5} \left(\frac{\mu_v}{2R_{\rm tube}}\right)^{1/5} {\rm Pr}^{-2/3}, \tag{12}$$

i.e, at fixed $J_{\rm strut}$ the heat transfer coefficient is proportional to $R_{\rm tube}^{-9/5}$ and, therefore, grows rapidly with decrease of $R_{\rm tube}$. Considering a tube of radius $R_{\rm tube} = 2$ mm, we find that for the mass flow given by Eq. (7) we have ${\rm Re}_{\rm tube} \simeq 10^4$ and ${\rm Pr}_{\rm tube} \simeq 0.8$, giving the Nusselt number ${\rm Nu}_{\rm tube} \simeq 32$ and the heat transfer coefficient $h_{\rm tube} \simeq 130$ W/(m^2·K) (using the parameters for GH2 at $T = T_{L0}$ and $p = p_1$ [49]). This corresponds to the power $P_{\rm loop} \simeq 4\pi^2 R_{\rm tube} R_{\rm strut} h_{\rm tube}(T_{s0} - T_{L0}) = 1.8$W taken away by the first loop of the tube, provided the strut at the base is at saturation temperature T_{s0}. Therefore, several loops are needed to take away the heat from the strut. Let us note that the pressure drop $\Delta p = p_1$ ensures the flow $J_{\rm strut}$ in a tube of length $L \simeq 200$ m (see Eq. (8)).

The analysis of heat exchange between the strut maintained at $T = T_0$ at the warm end and in thermal contact with cold GH2-carrying tubes is rather involved and is presented in Appendix A. The results depend significantly on many factors, including the dimensions and the material of the penetration. Similarly, the ability of the tube to take away the heat from the penetration depends in a non-trivial way on these factors, as we demonstrate below. For concreteness, in the following we will assume (nominal regime) that a thermally insulated tubular strut of radius $R_{\rm strut} = 10$ cm,

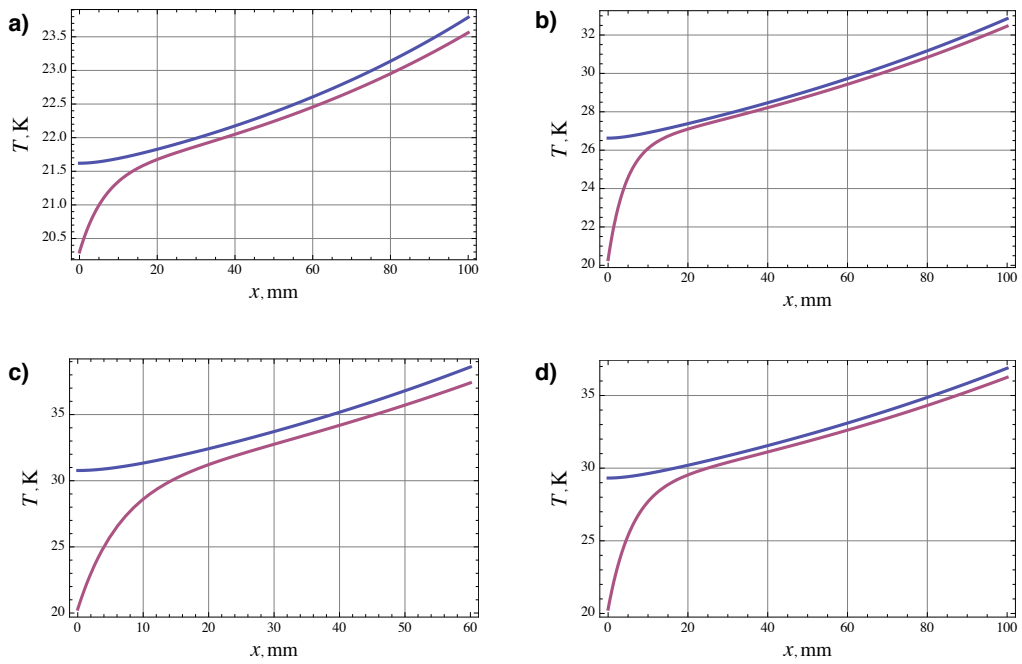

Figure 3. Temperature distributions in the strut (blue line) and the tube (purple line) as a function of the distance along the strut to the tank wall. (a) Nominal regime; (b) The strut radius is increased to $R_{\rm strut} = 15$ cm; (c) The strut is shortened to $L_{\rm strut} = 30$ cm; (d) The GH2 flow rate is decreased to $J_{\rm strut} = 2 \times 10^{-5}$ kg/s.

thickness $d_{\rm strut} = 5$ mm, length $L_{\rm strut} = 50$ cm is made of pure titanium and take the value of $\kappa_{\rm strut} \simeq 10$ W/(m·K) for thermal conductivity, corresponding to the low temperature end of this material parameter [37]. Under these assumptions, the heat leak through the strut in the absence of vapor cooling is equal to $Q_{\rm strut} = 15$W, consistent with the earlier discussion. We will also take the pitch of the helix $d_{\rm tube} = 2$ cm which is smaller than the strut radius and bigger than the tube diameter in order to ensure high surface area of thermal contact and absence of thermal shorts through the tubes.

The solution of the governing equations for the temperature distribution in both the strut and the tube as a function of the distance from the tank along the strut under an assumption that the tube captures all the heat entering into the strut at the warm end is presented in Fig. 3(a). One can see that a temperature boundary layer develops near the tank wall, in which the strut temperature fails to follow cold GH2 temperature on the length scale $l_{\rm strut} \simeq 2.5$ cm (see also the discussion in Appendix A). The maximum temperature at the strut base reaches 21.6K, which is still below the saturation temperature $T_{s0} = 22$K of LH2. Therefore, this rather crude analysis demonstrates that boiling at the attachment point of the strut may be suppressed by TVS-produced vapor cooling under suitable conditions.

Let us now see how sensitive this conclusion is to variations of various parameters of the considered cooling system. For example, consider the case in which the strut radius is increased by 50%. The solution of the governing equations is then presented in Fig. 3(b). One can see that in

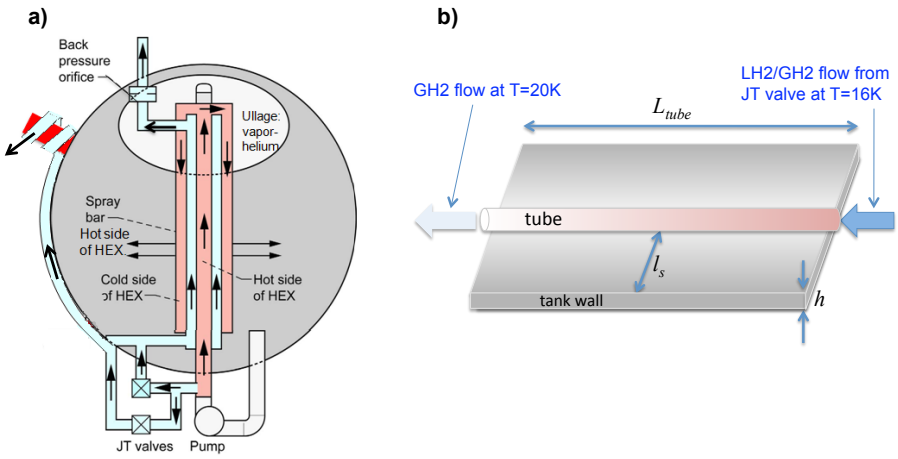

Figure 4. Cooling a penetration by LH2/GH2 mixture from TVS. (a) The tank schematics and (b) the details of the tube-to-tank scheme.

this case the strut base temperature increases to $T = 26.5$K, corresponding to a 4.5K superheat. Similarly, decreasing the strut length by 40% results in a strut base temperature $T = 31$K, a 9K superheat. Finally, a decrease of the GH2 supply rate by 40% results in the strut base temperature $T = 29$K, a 7K superheat. In all cases, the obtained superheat is big enough to initiate boiling. One should, therefore, carefully consider the heat conduction problem associated with penetrations in order to asses the feasibility of the proposed cooling strategy. One important factor to keep in mind is that, according to the model predictions, the efficiency of the proposed vapor cooling system decreases with an increase in the effective heat conductance coefficient of the strut. The latter must also include the effect of the additional heat conduction pathways introduced by the highly conducting thermal bonding material and the tubes themselves. It is not clear at this point whether this approach may always guarantee boiling suppression near the MLI penetration points. A more detailed and accurate analysis of the system is required.

Before concluding this section, we briefly comment on the possibility to use LH2 from the Joule-Thompson valve directly rather than GH2 from the TVS heat exchanger to cool the penetrations (see Fig. 4). This can be accomplished, e.g., by the tube-to-tank configuration, carrying the two-phase LH2/GH2 mixture from the Joule-Thompson valve to the penetrations. Let us point out in the first place that the added cooling power from the latent heat of LH2 is in fact only a small fraction of the total cooling power of the GH2 stream. Indeed, for the same reason that the use of VCS may potentially increase the heat leak capacity of the LH2 tank by a factor of 6 (see Sec. 3.1.4), the fraction of the latent heat of LH2 to the sensible heat of GH2, when heated from $T_{L0} = 20.3$K to $T_0 = 240$K is estimated to be $q_L J_{\rm strut}/(c_p(T_0 - T_{L0})) \simeq 0.2$. Therefore, the advantage of using LH2 rather than GH2 to cool the penetrations is rather questionable.

At the same time, in order to supply LH2 from the TVS output, the supply tubes must be sufficiently isolated to prevent boil-up and thermalization of the hydrogen flowing through the tubes with LH2 inside the tank. If not, LH2 will be transformed into GH2 due by the heat entering the tubes that carry the liquid from the Joule-Thompson valve towards the tubes wound around the strut (see Fig. 4). Indeed, the amount of heat entering a tube segment of length L may be estimated as $\kappa_w L h(T_{L0} - T_1)/l_s$, where κ_w is the tank wall thermal conductivity, h is the wall

thickness, and l_s is the length of temperature equilibration due to convection. In the presence of natural convection alone in microgravity the value of l_s may be estimated to be $l_s \simeq 1$ m (see Sec. 3.3.1 below for more detail), so for a highly conductive tank wall material with $\kappa_w = 200$ W/(m·K) and $h = 1$ cm we get that LH2 in the supply tube will boil completely on the length $L \simeq \eta q_L J_{\rm strut} l_s/(\eta \kappa_w h(T_{L0} - T_1)) \simeq 1.7$ m. Therefore, bringing LH2 from TVS to a penetration without thermal insulation of the tubes on the way is problematic. On the other hand, suppose that by using suitable thermal insulation the heat entering the supply tube on the way to the penetration to be cooled is reduced sufficiently, so that LH2 at $T_1 = 16$K is present at the first point of contact between the cooling tube and the penetration (see Fig. 2(b)). Then, since LH2 in the tube is significantly cooler than the surrounding LH2 in the tank and the tank walls, the tube may draw a substantial amount of heat from the tank wall rather than the penetration. It is possible to adapt the analysis of Appendix C (leading to Eq. (18) below) to show that a 4K subcooling of a strut base of radius $R_{\rm strut} = 10$ cm would result in a power $P \simeq 17$ W drawn from the wall, for the same tank wall parameters as above, in addition to $P_{\rm strut} = 15$W coming from the strut. This contradicts conservation of heat at the strut base. Therefore, the tube would not be able to cool the penetration, indicating that the tube temperature cannot be maintained at $T = T_1$. This, in turn, implies the onset of film boiling in the cooling tube, which would greatly reduce its heat transfer coefficient to the values characteristic of the use of GH2 vapor. Thus, the advantage of using LH2 is once again greatly diminished.

3.1.6 Helium dissolution hazard

We point out that at $T_{L0} = 20.3K$ the solubility limit of GHe in LH2 is ∼0.5% by weight [50]. Therefore, all LH2 in the tank is capable to absorb up to 75 kg of GHe, which is about 2 times more than the mass $M_{He} \simeq 35$ kg of GHe in the ullage at the beginning. Let us estimate the time in which GHe may dissolve in LH2. Taking the diffusion coefficient of the dissolved helium $D_{He} = 5 \times 10^{-9}$ m^2/s (assumed to be of the same order as the available value for neon [51], see also [52]), assuming that the ullage has the shape of a spherical bubble of radius $R_{g0} = 1.8$ m and estimating the diffusive flux at the ullage boundary to be $D_{He}\rho_{He,sat}/l_{He}$, where $\rho_{He,sat} = 0.005\rho_L$ is the helium saturation density and $l_{He} = \sqrt{D_{He}t}$ is the helium diffusion length, respectively, in LH2, we obtain that in the absence of active mixing the dissolved mass of GHe in time t is

$$M_{He,\rm dissolved} \simeq 4\pi R_{g0}^2 l_{He}\rho_{He,sat}, \qquad M_{He,\rm dissolved} \simeq 1.6 \text{ kg}, \quad t = 1 \text{ month}. \tag{13}$$

Let us note that in the presence of active mixing the rate of GHe dissolution may be significantly higher. For example, if LH2 is circulated with an average axial velocity $u_{bulk} = 1$ mm/s across the tank, then the Peclet number $\mathrm{Pe} = 2R_{g0}u_{bulk}/D_{He} \simeq 7 \times 10^5$ for the ullage bubble. Therefore, the dimensionless Sherwood number $\mathrm{Sh} = 0.65\mathrm{Pe}^{1/2} \simeq 550$ ([53, Eq. (3.52)], assuming spherical ullage in a background flow with velocity u_{bulk}), and the dissolution rate becomes $\dot{M}_{He} = 2\pi R_{g0} D_{He}\rho_{He,sat}\mathrm{Sh} \simeq 30$ kg/month. Thus, the entire mass of GHe may dissolve in LH2 in only one month, leading to the collapse of the ullage pressure. The dissolution rate may further increase due to ullage bubble motion. Therefore, on the long-term storage timescales one needs to evaluate the potential ullage collapse hazard due to GHe dissolution in LH2. One also needs to take into consideration the possible effect of dissolved non-condensible helium gas on the boiling characteristics [21, 54, 55].

3.2 Pressure control

When the sufficient level of superheat is reached at the tank walls and/or enough heat enters through penetrations, nucleate boiling will start. As vapor is created due to boil-off, the tank pressure rises, requiring venting in the absence of heat removal. As was shown in Sec. 3.1, with the considered heat leak the excess pressure $p_0 - p_{\rm atm}$ will increase by a factor of two in just 2 days in the absence of venting.

In microgravity, venting becomes and issue, since the location of the ullage space in the tank is not known and, therefore, it is not possible to guarantee that vapor, not liquid, is vented in the process. Note that venting LH2 caused the vehicle to tumble out of control during the AC-4 test flight in 1964 [8, 9]. To circumvent this problem, the thermodynamic vent system (TVS) technology is proposed, in which the two-phase mixture of liquid and vapor may be expanded in a Joule-Thompson device and then passed through a heat exchanger to take away heat from the warmer fluid in the tank, see Fig. 5 for schematics [6, 10, 31, 56]. We note that ideally the work of TVS would result in the LH2 loss rate equal to that of a tank with the same heat budget venting the vapor directly overboard. In practice, increased losses are inevitable due to finite TVS efficiency.

The basic physical principle of TVS operation is to control tank pressure by keeping the bulk LH2 at subcooled conditions. Therefore, successful operation of TVS relies crucially on its ability to efficiently move heat from the regions of nucleate boiling to the TVS heat exchanger inside the tank by utilizing fluid mixers, such as an axial jet or spray bars. We note that, on one hand, LH2 circulation must be sufficiently strong in order for the heat through penetrations to be removed from vapor bubbles. On the other hand, if the circulation is too strong, then the ullage bubble may be distorted or fragmented, resulting in its possible capture by the TVS intake, see Fig. 6.

3.2.1 TVS hazard induced by ullage motion

In microgravity the ullage containing the saturated vapor and helium can drift to the TVS intake and become captured by it. This dangerous effect is unexplored. It may cause the TVS to cease normal operation. Bubbles containing helium may come out of the TVS, decreasing the helium mass in the main ullage. These effects may cause generation of many new bubbles with GHe and the formation of the multi-phase liquid-gas foam instead of the regular ullage. It maybe then be impossible to annihilate this foam by pre-start pressurization, since the collapsing bubbles will contain non-condensible helium gas.

To estimate the critical LH2 circulation velocity u_{bulk}, above which the ullage motion hazard becomes significant, we compute the flow Weber number $\mathrm{We} = 2\rho_L u_{bulk}^2 R_{g0}/\sigma_L$. The flow will begin to affect the shape of the ullage bubble when the Weber number $\mathrm{We} \gtrsim 1$; for example, for $u_{bulk} = 0.5$ cm/s we will have $\mathrm{We} \simeq 4$, indicating the onset of ullage motion [19].

3.2.2 Boiling near hot spots

Let us now estimate the rate of heat removal from a bubble growing near a hot spot at the tank wall (Fig. 5(b) and Fig. 7). A detailed treatment of this question is difficult without specifics of the LH2 flow pattern, which depend on the tank design (see [32, 57] for recent numerical studies). Therefore, for simplicity we will assume that LH2 flow is generated by the axial jet which creates a counterflow pattern (see Fig. 5), in which LH2 moves with average velocity u_{bulk} in the region $r < R_0 - L$, where r is the distance to the tank axis, and with average velocity $u_{counter}$ in the

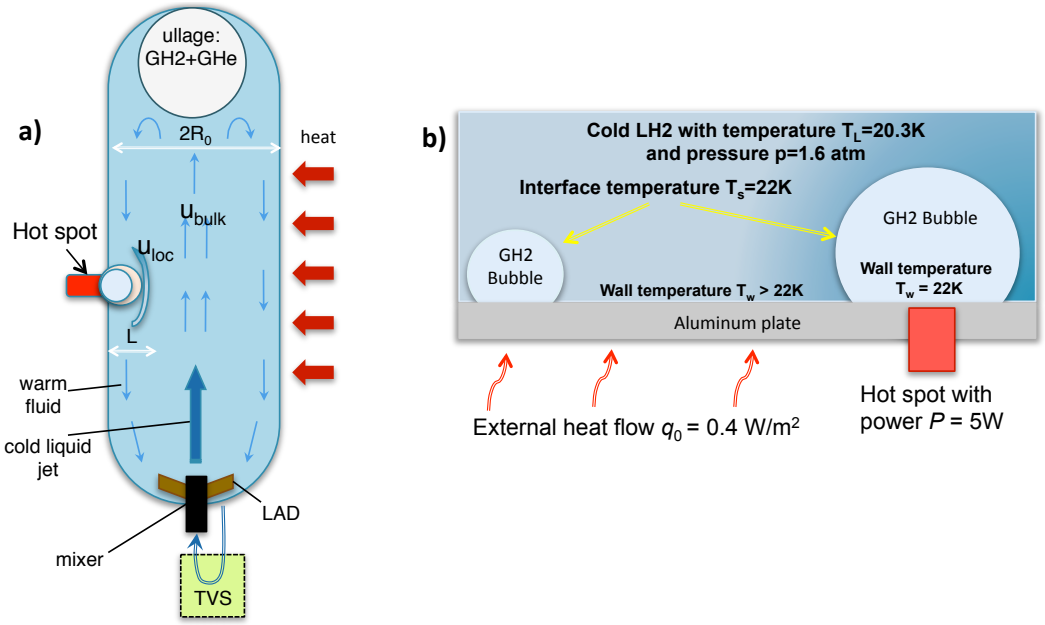

Figure 5. (a) A Tank/TVS configuration with an axial jet mixer. (b) Schematics of bubble growth on the tank wall. In (a), blue arrows indicate LH2 circulation; red arrows indicate heat influx through the MLI; on the left, a vapor bubble is attached to a hot spot (red) at the point of a localized heat leak through a penetration.

opposite direction in a layer of thickness L next to the tank wall. Since at the wall the flow velocity is zero, in a laminar flow the magnitude of the LH2 velocity next to a bubble of radius R may be estimated as $u_{loc} \simeq 4Ru_{counter}/L$, where we used linear interpolation from $u = 0$ at $r = R_0$ to $u = 2u_{counter}$ at $r = R_0 - L$ for the axial liquid velocity u. From mass conservation we find that

$$u_{loc} \simeq \frac{4R(R_0 - L)^2}{(2R_0 - L)L^2}\, u_{bulk}. \tag{14}$$

Taking $L \simeq 1$ m and the value of $u_{bulk} = 0.5$ cm/s obtained in the preceding paragraph, one can see that a localized heat source with power $P = 5$W may produce a steady bubble of radius $R \simeq 13$ cm. This follows from the balance of heat, taking into consideration that the Nusselt number $\mathrm{Nu}_R = P/(2\pi R\kappa_L(T_{s0} - T_{L0})) \simeq 35$ for the bubble can be correlated as $\mathrm{Nu}_R = 0.65\mathrm{Pe}_R^{1/2}$ with the Peclet number $\mathrm{Pe}_R = 2u_{loc}Rc_L\rho_L/\kappa_L \simeq 3000$ in this case (see [53, Eq. (3.52)]), assuming small contact angle and, hence, an almost spherical bubble, and ignoring the presence of the wall for the flow for simplicity). Similarly, a bulk velocity $u_{bulk} = 1$ mm/s would result in a steady bubble of radius $R = 20$ cm. We note that even with this smaller value of the circulation speed u_{bulk} one would need to supply LH2 through the axial jet at the rate $G_{LH2} = \pi(R_0 - L)^2\rho_L u_{bulk} \simeq 0.5$ kg/s, which, for an axial jet with an orifice of 10 cm diameter would require the fluid velocity of about 1 m/s. The corresponding circulation time for the whole tank would be 8 hours in this case. At the same time, for a given leak power the system will not be able to control the growth of bubbles attached to hot spots whose radii are smaller than the ones estimated above.

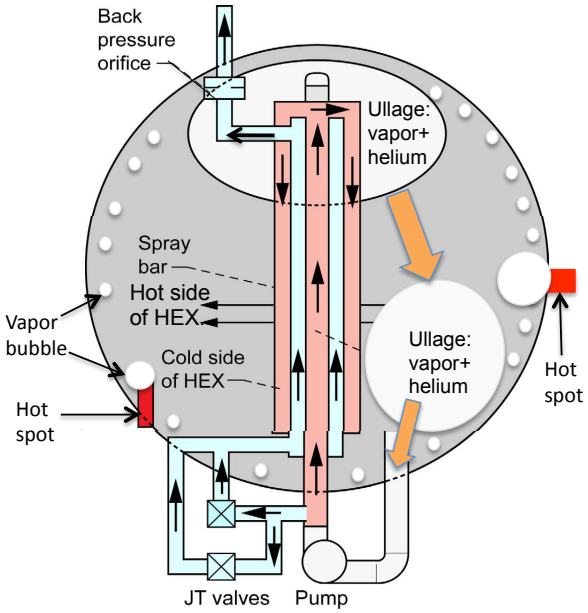

Figure 6. An illustration of the TVS hazard induced by ullage motion (spray bar TVS schematics adapted from [56]).

3.2.3 Formation of a multi-phase liquid-vapor foam

The above estimates assumed that the bubble receiving power P from the heat leak remains attached to the hot spot at all times. In microgravity, bubbles will have a much reduced tendency to detach from the wall and rise towards the ullage [21, 58–60]. Using the correlation of Fritz [17, 61], we find that the bubble radius at departure in microgravity can be estimated at $R_d \simeq 30$ cm, assuming, e.g., a contact angle $\gamma \simeq 20^\circ$ (small contact angles are characteristic of LH2, a strongly wetting liquid [61, 62]). Note that the Weber number for the bubble $\mathrm{We}_R = 2\rho_L u_{loc}^2 R/\sigma_L \simeq 0.005$ is small in this case, and so the bubble may not be blown off easily from the hot spot by the flow. If the bubble departure radius R_d exceeds the steady bubble radius obtained above, the bubble will stop growing and assume its steady-state radius, and the heat will be transferred from the hot spot through the bubble to the liquid, as desired.

The departure radius is proportional to the contact angle [17, 61] and becomes smaller than the steady-state bubble radius estimated in the preceding paragraph for contact angles $\gamma \lesssim 10^\circ$. Thus, for these smaller contact angles bubbles will be leaving the area of the hot spot and entering into the bulk liquid. Other mechanisms of bubble departure, such as bubble coalescence, g-jitter, and the effect of the liquid flow [17, 63, 64], which are found to be important under reduced gravity conditions [58–60], may further reduce the bubble departure radius. As a result, bubbles may be injected into the liquid and start to move with the flow, reaching, in particular, the flow stagnation regions. Continuously arriving and collapsing bubbles will raise the temperature in the stagnation regions above the subcooling temperature $T_{L0} = 20.3$K. As a result, the bubbles will stop collapsing and will accumulate in those regions. When bubbles arrive there, a complex multi-phase liquid-vapor foam-like mixture may form with temperature at saturation, $T_{s0} = 22$K. The bubble colonies

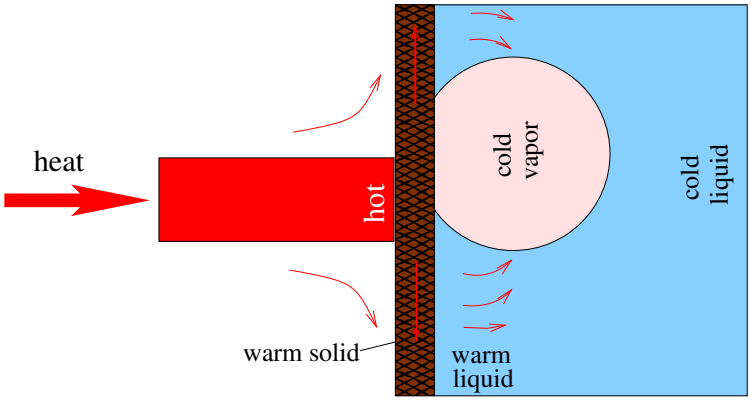

Figure 7. The schematics of the tank wall in contact with a heat leak. A vapor bubble grows by partially absorbing heat from the hot wall.

forming in this way may further thermally insulate the tank walls from the subcooled liquid and result in the formation of more bubbles through nucleate boiling, making TVS cooling ineffective.

3.3 Dynamics of bubble growth and collapse

We now discuss the dynamics of vapor bubbles inside LH2 in more detail.

3.3.1 Onset of bubble nucleations at hot spots

Let us begin by estimating the time needed for a single bubble to appear near a localized heat leak with power $P = 5$W. We assume that the heat enters the tank through a penetration connected to the exterior side of an aluminum LH2 tank. We note that in contrast to the Apollo design, in which thermal insulation was on the interior tank surface [16], the MLI has to be installed on the tank's exterior surface, since it needs to operate in vacuum. Hence, in the absence of any special inner surface coating, the stored LH2 will be in contact with a highly conductive metal surface. At $T_{L0} = 20.3$K, heat conductance κ_w of the tank wall lies in the range of 20 – 200 W/(m·K), depending on the composition of the aluminum alloy used [13, 65]. Also note that bubble inception superheat will be higher than the one needed to maintain nucleate boiling and will vary depending on the tank wall finish [21, 66–68].

Suppose first that LH2 is at the subcooled temperature T_{L0} when the heat leak is applied. Because of the much higher heat conductance of aluminum, this heat will first spread into the tank wall. If $l_w = \sqrt{\kappa_w t/(c_w \rho_w)}$ is the thermodiffusion length of aluminum, then one can roughly estimate the temperature increase in the tank wall by equating the amount of heat Pt entering aluminum in time t to the heat content $\pi l_w^2 h c_w \rho_w (T - T_{L0})$ of a cylindrical section of the tank wall with radius l_w and thickness h. The timescale of temperature spreading may also be estimated by equating l_w to r_0:

$$t_w = \frac{c_w \rho_w r_0^2}{\kappa_w} \simeq 0.3 \text{ s} \div 3 \text{ s}, \tag{15}$$

where $r_0 \simeq 5$ cm is the radius of the penetration. A more precise analysis (see Appendix B) gives

an extra logarithmic factor in the expression for the maximum temperature in the hot spot:

$$T \simeq T_{L0} + \frac{P}{4\pi h \kappa_w} \ln(at/t_w), \tag{16}$$

where $a \simeq 6.1$. Taking $h = 1$ cm, we find that for $t = 3t_w$ the value of T varies in the range 21K – 26K, depending on the heat conductance κ_w. Therefore, three distinct scenarios are possible, depending on the values of κ_w and P in the absence of boiling.

The first scenario is realized, if the heat leak power P is sufficiently high and the heat conductance κ_w is sufficiently low. For the considered value of P and $\kappa_w = 20$ W/(m·K), which is at the low end of the range of κ_w, by Eq. (16) we get $T \simeq 24$K already at $t = t_w = 3$ s. This corresponds to superheat of 2K, already above the nominal 1K superheat for the nucleate boiling onset in LH2 [41–43]. In this situation, nucleate boiling will start immediately, with all the heat going into a single vapor bubble.

The second scenario is realized when the heat conductance κ_w is sufficiently high. Then in the presence of losses through convection the heat from the leak spreads to distances up to (see Appendix C)

$$l_s = \sqrt{\frac{\kappa_w h R_0}{\kappa_L \mathrm{Nu}_{R_0}}}, \tag{17}$$

where Nu_{R_0} is the Nusselt number associated with convection. The maximum temperature in the hot spot can be estimated as (see Appendix C)

$$\max T \simeq T_{L0} + \frac{P}{2\pi \kappa_w h} \ln\left(\frac{b l_s}{r_0}\right), \tag{18}$$

where $b \simeq 1.85$. For example, with $\kappa_w = 200$W/(m·K), corresponding to the high end of the range of κ_w, and $\mathrm{Nu}_{R_0} \simeq 46$ estimated in Sec. 3.1 for free convection in microgravity, we obtain $l_s \simeq 1$ m. About the same Nusselt number is also obtained for forced convection with average velocity $u_{bulk} = 1$ mm/s considered in Sec. 3.1, using the correlation [44, Eq. (7.23)]

$$\mathrm{Nu}_{R_0} = 0.332 \times \left(\frac{\rho_L u_{bulk} R_0}{\mu_L}\right)^{1/2} \left(\frac{c_L \mu_L}{\kappa_L}\right)^{1/3} \simeq 44. \tag{19}$$

Then, according to Eq. (18), we get $\max T \simeq 21.8$K, so the temperature in a hot spot remains below the saturation temperature, and the heat is removed convectively from the leak, as desired. Note that in zero gravity and absence of any boiling or mixing the value of l_s in Eq. (18) should be replaced with R_0, and the value of T_{L0} should be replaced with the spatially averaged tank temperature T_{w0}. The latter will be increasing on the timescale $t_{\mathrm{sat,thermodiffusion}}$ (see Sec. 3.1), eventually leading to nucleate boiling. On the other hand, an addition of an active mixer next to a hot spot will further reduce the value of l_s and, therefore, further suppress boiling. This may be a better strategy for mitigating the effect of heat leaks through MLI penetrations (compare with the strategies discussed in Sec. 3.1.5).

The third scenario is realized when the wall heat conductance is low, and the heat leak power is also sufficiently low, provided that convective heat transfer is negligible. The latter takes place, e.g., in zero gravity and in the absence of active mixing. We consider this scenario in more detail in Sec. 3.3.2.

3.3.2 Explosive nucleate boiling hazard

If the power P is not sufficient to initiate nucleate boiling quickly in time t_w, then, according to Eq. (16) it may take an exponentially long time for the wall temperature to reach the required superheat, resulting in a long delay in the onset of nucleate boiling. Consider, for example, the case of $\kappa_w = 20$ W/(m·K) and $P = 1$W. Then, by Eq. (16) a temperature $T \simeq 24$K corresponding to a 2K superheat will only be reached at $t = 1.4$ hours. In this time the heat will spread to $l_w \simeq 2$ m along the tank wall and $l_L \simeq \sqrt{\kappa_L t/(c_L \rho_L)} \simeq 2.6$ cm into LH2. When nucleation occurs, the heat stored in this superheated layer of LH2 will be used to convert a mass m_{H2} into vapor, with $m_{H2} \simeq \pi l_w^2 l_L c_L \rho_L (T - T_{s0})/q_L = 1$ kg for the considered parameters. The resulting vapor volume $V \simeq 0.5$ m^3 will then be violently released into the tank in a short time. This is an example of the phenomenon of explosive nucleate boiling [67–69] that was ubiquitously observed in the microgravity boiling experiments on board the Space Shuttle Columbia [40]. We note that the accompanying pressure spike may present a potential hazard for the operation of the storage tank. Moreover, many vapor bubbles may be injected into LH2 as a consequence of explosive boiling, contributing to the formation of liquid-vapor foam.

Let us note that in the absence of mixing the size of the hot spot is limited by the length scale (see Appendix D)

$$L = \frac{\kappa_w}{\kappa_L} h. \tag{20}$$

Assuming that $\kappa_w \simeq 20$ W/(m·K), as before, we find that $L \simeq 2$ m. Correspondingly, the maximum temperature in the hot spot is limited by the expression given by Eq. (18) with l_s replaced by L (see Appendix D). However, in this case the steady state superheat will extend into the liquid also to the length L, creating a much larger mass of superheated LH2, whose explosive boiling may lead to catastrophic consequences.

3.3.3 Bubble growth over a hot spot

Once a vapor bubble is nucleated, it will grow by drawing the heat from surrounding superheated liquid which, in turn, receives heat from hot spots on the tank wall. We note that for small heat fluxes considered here the dominant heat transfer mechanism will be transient heat conduction (for a recent discussion of different growth mechanisms, see [70]).

Assuming that all the power from a localized heat leak is used to convert liquid into vapor in a single bubble, the bubble radius as a function of temperature, or, equivalently, the growth time for a bubble of a given radius, are given by

$$R = \left(\frac{3Pt}{4\pi \rho_v q_L} \right)^{1/3}, \qquad t_{\rm growth} = \frac{4\pi \rho_v q_L R^3}{3P}. \tag{21}$$

With $P = 5$W, we then find

$$R \simeq 20 \text{ cm}, \quad t_{\rm growth} = 1.7 \text{ hour}, \qquad\qquad R \simeq 2 \text{ cm}, \quad t_{\rm growth} = 6 \text{ seconds}. \tag{22}$$

Note the difference in the dependence of the bubble radius R on t with the classical $t^{1/2}$ dependence obtained in [71, 72] (see also [62, 64]). This is due to the fact that the bubbles under consideration grow near a hot spot on a thin strongly conductive tank surface. Therefore, heat flux into the

bubble is mediated by the high heat conductance through the tank wall (for a recent discussion of the importance of heat conductance in the heater during nucleate boiling, see [73–75]; see also Sec. 4.2).

Note that far from the hot spots this formula remains valid, if one sets $P = q_0 A$, where A is the wall area per single bubble. The latter is valid in the case of high heat conductance of the tank wall, when on average each bubbles will be able to intercept all the heat entering through the area A of the tank wall. For example, for $A = L^2$, with $L = 10$ cm, we find that the bubbles will reach the radius of $R = 2$ cm in $t \simeq 2$ hours. When neighboring bubbles at the tank wall grow large enough to come in contact with each other, more complicated dynamics involving coalescence and detachment from the tank wall will occur.

3.3.4 Bubble collapse and accumulation in the subcooled liquid

As a result of several possible bubble departure mechanisms, vapor bubbles may detach from the tank wall and enter into the bulk liquid. Several scenarios are possible here, depending on the size of the departing bubbles, the level of microgravity, and the liquid flow rate. Larger bubbles may rise toward the area of zero gravity (the tank mid-plane for a tank in a circular LEO) under the action of buoyancy forces. The rise time may be estimated by balancing the buoyancy force $\frac{4}{3}\pi R^3 \rho_L g$ with viscous drag $4\pi\mu_L R u$, where $u \simeq R_0/t_{\rm rise}$ is the bubble velocity relative to the liquid (recall that R_0 is the tank radius) [53], to obtain

$$t_{\rm rise} = \frac{3\mu_L R_0}{\rho_L g R^2} \simeq 5 \text{ min}, \qquad R = 2 \text{ cm}, \tag{23}$$

which is decreasing with the increase of bubble radius R. These bubbles may then be swept towards the ullage bubble by the flow generated by the mixer and coalesce with it (see Fig. 5). The timescale of this process is given by

$$t_{\rm flow} = \frac{H_0}{u_{bulk}} \simeq 3 \text{ hours}, \qquad u_{bulk} = 1 \text{ mm/s}. \tag{24}$$

Note that by Eq. (22) it takes much longer for a bubble to reach the ullage than to grow to the considered size. Hence bubbles may accumulate in the liquid and be carried along by the flow and deposited in its stagnation areas.

Let us now estimate the bubble lifetime, assuming that upon departure it enters the region of the subcooled LH2. Assuming first that the heat escapes the bubble via steady conduction and equating the conductive heat flow $4\pi R^2 \kappa_L (T_{s0} - T_{L0})/R$ to the heat release rate $4\pi R^2 (dR/dt)\rho_v q_L$ due to condensation, and then solving the obtained differential equation, we obtain the time for the bubble of radius R to collapse into the subcooled liquid:

$$t_{\rm collapse1} = \frac{q_L \rho_v R^2}{2\kappa_L (T_{s0} - T_{L0})}. \tag{25}$$

Note that this equation is asymptotically exact in the limit of vanishing subcooling, but underestimates $t_{\rm collapse1}$ for larger subcoolings due to the condensation blocking effect [76]. Indeed, assuming that the condensation rate is dominated by the conduction through the thermal boundary layer of width $l = \sqrt{\kappa_L t/(c_L \rho_L)}$ and, hence, one should replace the factor $1/R$ by $1/l$ in the expression for

the heat flux (a more precise analysis, also giving the coefficient of proportionality is presented in Appendix E)

$$t_{\text{collapse2}} = \frac{\pi \rho_v^2 q_L^2 R^2}{4 c_L \rho_L \kappa_L (T_{s0} - T_{L0})^2}. \tag{26}$$

The blocking mechanism is not important when $t_{\text{collapse1}} \lesssim t_{\text{collapse2}}$, which is the case in the examples that follow.

From Eq. (25), one can see that a bubble of radius $R = 20$ cm will have a lifetime $t_{\text{collapse1}} \simeq 30$ hours ($t_{\text{growth}} \simeq 1.7$ hour). For smaller bubbles with, say, $R = 2$ cm, we have $t_{\text{collapse1}} \simeq 20$ mins ($t_{\text{growth}} \simeq 6$ sec). Note that these estimates agree very well with the results of direct numerical simulations of the full system of hydrodynamic equations describing the bubble collapse which are presented in Sec. 5. Once again, in the considered case the bubbles are produced faster than they are collapsing in the subcooled liquid, i.e. $t_{\text{growth}} \ll t_{\text{collapse}}$. Note, however, that as the bubbles collapse, they release heat into the liquid, so that the subsequent bubbles are exposed to a smaller degree of subcooling. Therefore, as more bubbles arrive, their lifetime may steadily increase and the liquid around them reach saturation, resulting in the formation of stable bubble colonies. These colonies then contribute to the formation of the multiphase liquid-vapor foam.

3.3.5 Bubble collapse by pre-start pressurization

The presence of vapor bubbles in LH2 is highly undesirable for the engine restart, since those bubbles may enter into engine feed lines and result in cavitation of the turbopumps [1]. A way to reduce or eliminate the vapor bubbles prior to engine restart is to pressurize the tank with GHe and, at the same time, apply a small settling thrust from ullage engines. Pressurization changes the LH2 saturation temperature relative to the bulk liquid temperature, making vapor bubbles to condense.

Several issues arise in the course of pre-start pressurization which may result in an incomplete vapor bubble collapse, making the procedure inefficient. First, bubble condensation releases heat into the bulk liquid, increasing its temperature and potentially bringing it to the new saturation temperature and stopping further condensation. This is particularly relevant to the vapor bubble colonies. Consider, for example, the case in which the tank originally at pressure $p_0 = 1.6$ atm is pressurized to a new pressure $p = 2$ atm. The corresponding new saturation temperature is $T_s = 23$K. Now, suppose a bubble colony, which remains at the old saturation temperature $T_{s0} = 22$K has vapor volume fraction f. Then the total amount of heat this foam-like multiphase fluid can absorb is

$$Q = (1 - f) c_L \rho_L V (T_s - T_{s0}), \tag{27}$$

where V is the colony volume. This amount of heat, in turn, can condense only the volume $V_{cond} = Q/(q_L \rho_v)$ of the vapor. Comparing the value of V_{cond} with the total vapor volume fV, we can see that by purely thermodynamic considerations all the bubbles will not be able to condense, if

$$f \geq \left(1 + \frac{\rho_v q_L}{c_L \rho_L (T_s - T_{s0})}\right)^{-1} \simeq 0.45. \tag{28}$$

In other words, it will not be thermodynamically possible to condense all the vapor, if the volume fraction of vapor exceeds a critical value given by Eq. (28).

On the other hand, even if the volume fraction f of vapor is below the critical value, vapor condensation may not occur during the time interval of pressurization due to the general slowness of the condensation process and, in particular, due to the condensation blocking phenomenon for larger bubbles. One can once again use Eqs. (25) and (26) in these two regimes to estimate the collapse time for bubbles of different size, provided that $T_{s0} - T_{L0}$ is replaced with $T_s - T_{s0}$. Using these formulas, we now find that

$$t_{\rm collapse1} = 30 \text{ mins}, \quad R = 2 \text{ cm}, \qquad\qquad t_{\rm collapse1} = 50 \text{ hours}, \quad R = 20 \text{ cm}. \tag{29}$$

It is clear that larger bubbles may not be eliminated by pressurization in a reasonable time. However, by a settling acceleration $g \sim 10^{-4} g_0$ it is possible to move larger bubbles toward the ullage. Using Eq. (23) with R_0 replaced by H_0, we find that bubbles of radii $R \geq 5$ mm will be able to move towards the ullage in time $t_{\rm rise} = 5$ mins. At the same time, for smaller bubbles the collapse time is bounded above by $t_{\rm collapse1} \simeq 2$ mins, assuming the best case scenario given by Eq. (25). This indicates that there are rather tight constraints for achieving the desired result from pre-start pressurization. Also note that during pre-start pressurization bubbles will be continuously generated at the hot spots. Provided their departure radius is below 5 mm, these bubbles will not be eliminated at the moment of engine start. In addition, larger bubbles forming inside the engine's start box, if any, will be trapped by the capillary screens of the liquid acquisition device (LAD) and will not be able to rise to the ullage. Finally, helium-filled bubbles forming as a result of a possible ullage capture by the TVS intake cannot be eliminated by pre-start pressurization.

4 Mathematical models of bubble dynamics

Here we present a discussion of more detailed mathematical models that can be used for the analysis of heat transfer mechanisms and bubble growth and interaction in microgravity under heat loads relevant for long-term cryogenic storage.

4.1 Conductance-based models

Consider a situation in which bubbles form due to boil-off at the tank wall in the vicinity of a heat leak in a quiescent saturated liquid (Fig 7). In the absence of vapor bubbles the heat from the localized heat leak will enter into the tank wall and rapidly spread along the wall. When the heat spreads sufficiently far from the source, it will then start entering into the liquid inside the tank. Mathematically, this can be described by the following equations (for simplicity, we neglect the temperature dependence of all the material parameters and assume that the liquid occupies a semi-infinite space next to the flat tank wall):

$$c_w \rho_w \frac{\partial T}{\partial t} = \kappa_w \left(\frac{\partial^2 T}{\partial x^2} + \frac{\partial^2 T}{\partial y^2} \right) + \frac{\kappa_L}{h} \frac{\partial T}{\partial z} + \frac{1}{h} q(x, y, t), \qquad z = 0, \tag{30}$$

$$c_L \rho_L \frac{\partial T}{\partial t} = \kappa_L \left(\frac{\partial^2 T}{\partial x^2} + \frac{\partial^2 T}{\partial y^2} + \frac{\partial^2 T}{\partial z^2} \right), \qquad z > 0, \tag{31}$$

where the first equation is the heat conductance equation in the wall, averaged over the wall thickness h (see [77] for a similar treatment), assuming the wall coincides with the plane $z = 0$, and

the second equation is the equation of heat conductance in the liquid. The two equations above are coupled via the boundary condition, namely, via continuity of temperature T at $z = 0$, and the derivative $\partial T/\partial z$ is evaluated as $z \to 0^+$. The quantity q appearing in Eq. (31) represents the heat flux from a localized heat source. In writing the above equations we neglected the possible convective terms (including thermocapillary forces [54, 55, 58, 59, 78]), which are expected to be quite small under the considered heat loads. For example, in the case of a bubble of radius $R = 2$ cm and heat penetration length $l \simeq 2R$, the associated Rayleigh number is

$$\mathrm{Ra} = \frac{g\beta_L(T_{s0} - T_{L0})c_L\rho_L^2 l^3}{\mu_L\kappa_L} \simeq 900, \tag{32}$$

which is not sufficient for the onset of microconvection [79].

4.2 Bubble growth as function of bubble location

Vapor bubbles play the role of heat sinks for the heat conductance problem in Eqs. (30) and (31), and will, therefore, screen the heat coming from the wall into the bulk liquid (for a recent review of single bubble heat transfer mechanisms, see [70]). To incorporate the bubbles, we need to introduce the boundary condition $T = T_s(p)$, where T_s is the saturation temperature at the ambient pressure p, at the boundary of each bubble. As a consequence, heat will flow in or out of each bubble, making them grow or shrink, respectively. Under the considered conditions of very slow dynamics (on the time scale of hours or greater), the growth of a vapor bubble will be thermally-limited [71, 72], with transient conduction dominating other possible heat transfer mechanisms [70]. For a spherical bubble (assuming zero contact angle for simplicity) this leads to

$$4\pi\rho_v q_L R^2 \frac{dR}{dt} = Q, \qquad Q = \kappa_L \int_{\partial B} \frac{\partial T}{\partial \nu}\, dA, \tag{33}$$

where ∂B denotes the boundary of the bubble, $\partial/\partial\nu$ is the derivative in the direction of the outward normal to ∂B. Moreover, since the underlying conductance-limited bubble growth dynamics will be slow, it is reasonable to adopt a quasi steady-state approximation in solving Eqs. (30) and (31). This approximation will be valid when the time scale of thermal diffusion exceeds that of conductance-mediated growth. Estimating these timescales:

$$t_{\text{thermodiffusion}} = \frac{c_L\rho_L R^2}{\kappa_L}, \qquad t_{\text{conductance}} = \frac{q_L\rho_v R^2}{\kappa_L(T - T_s)}, \tag{34}$$

one can see that the condition $t_{\text{conductance}} \gtrsim t_{\text{thermodiffusion}}$ is roughly satisfied for superheats under 1K in LH2.

Consider now an isolated bubble with the center $\mathbf{r}_0$ which is at least distance $d > R$ away from the wall. It is then possible to use the method of images [80] to express the solution of the obtained elliptic boundary value problem in the form of an infinite series:

$$T(\mathbf{r}) = T_s(p) + \frac{1}{2\pi\kappa_L} \sum_{n=1}^{\infty} \int_{\text{wall}} \frac{q_n(\mathbf{r}')}{|\mathbf{r} - \mathbf{r}_n(\mathbf{r}')|}\, d^2r'. \tag{35}$$

Here

$$q_1(\mathbf{r}') = \tilde{q}(\mathbf{r}'), \qquad \mathbf{r}_1 = \mathbf{r}', \qquad \tilde{q} = -\kappa_L \left.\frac{\partial T}{\partial z}\right|_{z=0}, \tag{36}$$

$$q_{n+1}(\mathbf{r}') = -\frac{R q_n(\mathbf{r}')}{|\mathbf{r}_n(\mathbf{r}') - \mathbf{r}_0|}, \qquad \mathbf{r}_{n+1}(\mathbf{r}') = \mathbf{r}_0 + \frac{R^2(\mathbf{r}_n(\mathbf{r}') - \mathbf{r}_0)}{|\mathbf{r}_n(\mathbf{r}') - \mathbf{r}_0|^2}, \qquad n \text{ odd}, \tag{37}$$

$$q_{n+1}(\mathbf{r}') = q_n(\mathbf{r}'), \qquad \mathbf{r}_{n+1}(\mathbf{r}') = P\mathbf{r}_n(\mathbf{r}'), \qquad n \text{ even}, \tag{38}$$

where P is the mirror reflection with respect to the xy-plane. In view of the fact that $q_{n+2}/q_n \leq R/d < 1$, the series in Eq. (35) converges exponentially fast. Furthermore, by Gauss theorem, the total heat flow Q into the bubble is given explicitly by

$$Q = -2\sum_{n=1}^{\infty} \int_{\text{wall}} \tilde{q}_{2n}(\mathbf{r})\, d^2 r. \tag{39}$$

This expression may then be substituted into Eq. (33), which gives an equation for the bubble radius in terms of the flux $\tilde{q}$ from the wall to the liquid. This flux, in turn, can be found by solving the integral equation obtained by plugging the wall temperature, obtained from Eq. (35), into Eq. (30) with the time derivative set to zero.

To get a sense of the phenomena described by the equations obtained above, let us consider a situation, in which a large bubble is suspended in the liquid at a distance d from the wall, such that $R \ll d \ll L$, where L is defined in (20), directly over a point heat source $q(x, y) = P\delta(x)\delta(y)$. Then it is possible to retain only the first term in the series in Eq. (35). This allows one to estimate Q as follows

$$Q \sim \frac{R}{d}\tilde{q}d^2 \sim \frac{PRd}{L^2}, \tag{40}$$

where we took into account that $\tilde{q} \sim P/L^2$ and that only the region of size of order d will give a significant contribution to the integral in (39). According to Eqs. (33) and (20), this implies that the bubble will grow on the time scale $t \sim \rho_v q_L R^2 \kappa_w^2 h^2/(Pd\kappa_L^2)$. Taking $R \sim d \sim 1$ cm and $P \sim 1$ W, we can estimate $t \sim 10$ hours for $\kappa_w = 20$ W/(m·K). On the other hand, if $d \to R$, the entire flux P will be absorbed by the bubble, giving a much faster time scale of growth $t = 4\pi\rho_v q_L R^3/(3P)$ (i.e. Eq. (21)), and for $R = 1$ cm we now have $t \sim 4$ s. Thus, the timescales associated with the bubble dynamics depend sensitively on the bubble location.

4.3 Interaction of bubbles

From the arguments leading to Eq. (40), it is clear that many bubbles may need to be created to take away the heat entering the tank from a localized heat leak. In principle, it is possible to use the approach of Sec. 4.2 to incorporate the effect of multiple bubbles on heat transfer. However, with the number of bubbles rapidly increasing, the problem of calculating the series representation of the temperature distribution quickly becomes intractable. Instead, a homogenization approach which reduces the bubble-filled liquid to an effective medium is advantageous (for a general reference, see e.g. [81]). Note that a related class of problems was recently treated by homogenization techniques in [82].

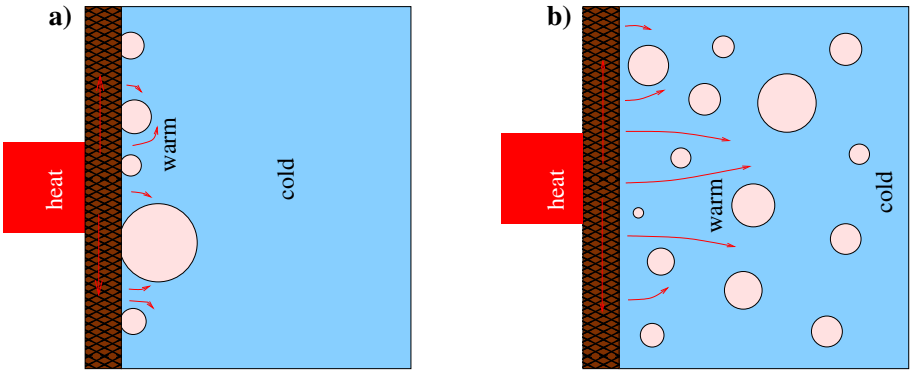

Figure 8. Multiple bubbles attached to the wall (a) or inside the liquid (b).

There are two main situations that need to be considered (see Fig. 8). In the first, it is assumed that only bubbles attached to the wall are present (Fig. 8(a)). In this case each bubble will work as a sink absorbing a heat flow $Q_R = C_R \kappa_w h(T - T_s)/\ln(l/R)$, where $l \gg R$ is the characteristic distance between bubbles and C_R is a constant that needs to be obtained from the solution of the homogenization cell problem. Introducing the distribution function $f_2(R, \mathbf{r}, t)$ which gives the number of bubbles of radius between R and $R + dR$ in the wall area element d^2r around $\mathbf{r}$ at time t, we then find that the averaged heat flow into the bubble per unit wall area is

$$\bar{Q}(\mathbf{r}, t) = K_2(\mathbf{r}, t)(T(\mathbf{r}) - T_s), \qquad K_2(\mathbf{r}, t) = \kappa_w h \int_0^\infty \frac{C_R}{\ln(l/R)} f_2(R, \mathbf{r}, t) dR, \tag{41}$$

where K_2 is the effective (homogenized) heat transfer coefficient in two dimensions. Substituting this formula into Eq. (30), we now obtain the respective homogenized equation for the wall temperature

$$c_w \rho_w \frac{\partial T}{\partial t} = \kappa_w \left(\frac{\partial^2 T}{\partial x^2} + \frac{\partial^2 T}{\partial y^2} \right) - \frac{K_2(\mathbf{r}, t)}{h}(T - T_s) + \frac{1}{h} q(x, y, t). \tag{42}$$

If all the bubbles have the same radius R, and the spatial density of bubbles is constant equal to $c_2 = 1/l^2$, then the coefficient K_2 becomes

$$K_2 = \frac{2 c_2 \kappa_w h C_R}{|\ln(c_2 R^2)|}. \tag{43}$$

From this equation, one can obtain the screening length $\lambda_2 \sim \sqrt{h\kappa_w / K_2} \sim l \ln^{1/2}(l/R)$. This will be the length scale of spreading of heat from a heat leak in the presence of bubbles attached to the wall.

In the second scenario one needs to consider bubbles suspended in the liquid. The homogenization problem in this situation (with fixed bubbles) was solved in Ref. [83]. The resulting homogenized version of Eq. (31) becomes

$$c_L \rho_L \frac{\partial T}{\partial t} = \kappa_L \left(\frac{\partial^2 T}{\partial x^2} + \frac{\partial^2 T}{\partial y^2} + \frac{\partial^2 T}{\partial z^2} \right) - K_3(\mathbf{r}, t)(T - T_s), \tag{44}$$

where, introducing the distribution function $f_3(R, \mathbf{r}, t)$ of bubbles of radius between R and $R + dR$ in the volume element d^3r, we get

$$K_3(\mathbf{r}, t) = 4\pi\kappa_L \int_0^\infty R f_3(R, \mathbf{r}, t) dR. \tag{45}$$

Once again, if $c_3 = 1/l^3$ is the constant density of bubbles inside the liquid, we find

$$K_3 = 4\pi\kappa_L R c_3, \tag{46}$$

and the respective screening length is $\lambda_3 \sim \sqrt{\kappa_L/K_3} \sim l\sqrt{l/R}$.

One can further use the expressions obtained above to find the effective heat transfer coefficient K_2 appearing in Eq. (42). Assuming that T varies on a much longer spatial scale than λ_3, we can reduce Eq. (44) to a one-dimensional boundary value problem (also taking advantage of the quasi steady-state approximation). As a result, the solution for T (homogenized) in the liquid may be written as

$$T(x, y, z) \simeq T_s + (T(x, y, 0) - T_s)e^{-z/\lambda_3}, \qquad \lambda_3 = \left(4\pi \int_0^\infty R f_3(R) dR\right)^{-1/2}, \tag{47}$$

where we assumed for simplicity that the bubble distribution is constant in space and time. Plugging this expression into Eq. (30), we obtain Eq. (42) with

$$K_2 = \frac{\kappa_L}{\lambda_3}, \tag{48}$$

giving the screening length in the plane $\lambda_2 \sim \sqrt{h\lambda_3\kappa_w/\kappa_L} = \sqrt{L\lambda_3}$. The problem needs to be studied further when both mechanisms of heat transfer act simultaneously.

4.4 Ostwald ripening

Let us now discuss a possibility of Ostwald ripening in the suspension of bubbles inside the liquid or a collection of bubbles attached to the wall [66]. In microgravity, an intriguing new mechanism may result in Lifshitz-Slyozov-type dynamics of vapor bubbles, even in the absence of mass transport between bubbles. Instead, the mechanism can be mediated via temperature, as we demonstrate below. Due to surface tension, the vapor pressure inside a bubble of radius R is equal to $p = p_0 + 2\sigma_L/R$ [84]. At the same time, in order to achieve evaporation-condensation equilibrium, the vapor pressure must be equal to the saturation pressure at temperature on the bubble wall. This leads to a peculiar feedback mechanism: The temperature on the surface of a smaller bubble with radius R_1 is higher than that on the surfaces of a larger bubble with radius R_2:

$$T_1 > T_2 \ \text{ if } \ R_1 < R_2, \qquad T_{1,2} = T_s + \frac{2T_s\sigma_L}{q_L\rho_v R_{1,2}}, \tag{49}$$

where we used the Clapeyron-Clausius relation [84]. As a consequence, heat will flow from the smaller bubble to the larger one, resulting in condensation in the smaller bubble and evaporation in the larger bubble under suitable conditions. It is possible to show that the resulting problem is mathematically equivalent to the one describing Ostwald ripening during solute precipitation in a supersaturated solution and can, therefore, be described within the Lifshitz-Slyozov theory [85].

Estimating the time scale of ripening by balancing the amount of heat $4\pi R^2 \rho_v q_L dR$ needed to increase the bubble radius by dR with the inflow of heat $4\pi R^2 \kappa_L T_s \sigma_L/(q_L \rho_v R^2) dt$ in time dt, we obtain

$$t_{\text{ripening1}} \simeq \frac{\rho_v^2 q_L^2 R^3}{\kappa_L \sigma_L T_s}, \tag{50}$$

and the usual Lifshitz-Slyozov $R \sim t^{1/3}$ growth law. For LH2, we find that this process is quite slow in the case of bubbles suspended in the liquid, with $t_{\text{ripening1}} \sim$2.5 days for bubbles of average radius $R \sim 1$ mm. At the same time, if the bubbles are attached to the highly conducting tank wall, then the heat conductance between the bubbles is enhanced, with the heat flow into the bubble of order $2\pi R h \kappa_w T_s \sigma_L/(q_L \rho_v R^2) dt$, resulting in an estimate

$$t_{\text{ripening2}} \simeq \frac{\rho_v^2 q_L^2 R^4}{h \kappa_w \sigma_L T_s}, \tag{51}$$

and an unusual dependence $R \sim t^{1/4}$. Once again, using $h = 1$ cm and $\kappa_w = 200$ W/(m·K) for highly conductive tank wall material, we obtain $t \simeq 20$ days for $R = 2$ cm. Therefore, the latter ripening mechanism may play an important role in selecting the bubble sizes.

4.5 Motion of bubbles suspended in the liquid

Let us now discuss the motion of bubbles under the action of microgravity. Let $\mathbf{g}(\mathbf{r}, t)$ denote the apparent acceleration of gravity in the tank (which includes forces of inertia). Note that both the direction and the magnitude of the vector $\mathbf{g}$ may vary in space and time. Since the magnitude of $\mathbf{g}$ is very small, the movement of bubbles will be dominated by viscous drag. An isolated bubble away from the walls will, therefore, move with velocity [53, Eq. (3.15)]

$$\mathbf{v} = \mathbf{u} - \frac{\rho_L R^2}{3\mu_L} \mathbf{g}, \tag{52}$$

where $\mathbf{u}$ is the background liquid velocity, and we neglected the vapor density compared to ρ_L. Note that when $|\mathbf{g}| \sim 10^{-5}$ m/s^2 and $R \sim 1$ cm, the bubble would move with speed $|\mathbf{v}| \sim 2$ mm/s in LH2, comparable to the characteristic fluid circulation velocities considered in Sec. 3.2.2. In the case of many hydrodynamically non-interacting bubbles, one can use this equation for $\mathbf{v}$, together with Eq. (33), to write the continuity equation for the bubble density $f_3(R, \mathbf{r}, t)$:

$$\frac{\partial f_3}{\partial t} + \nabla \cdot \left\{ \left(\mathbf{u} - \frac{\rho_L R^2}{3\mu_L} \mathbf{g} \right) f_3 \right\} + \frac{\partial}{\partial R} \left(\frac{Q}{4\pi \rho_v q_L R^2} f_3 \right) = D \nabla^2 f_3. \tag{53}$$

The heat flow Q, in turn, depends on R and the temperature distribution in the liquid, obtained, e.g. by solving the homogenized Eq. (44). In writing Eq. (53) we also introduced an effective diffusion constant D depending on R which possibly arises due to turbulence or vibrations (the g-jitter is not included in $\mathbf{g}$). Finally, note that the bubbles, in turn, will exert a body force onto the liquid and may, therefore, affect the flow.

4.6 Bubble creation and departure from the wall

Equation (53) needs to be supplemented with boundary conditions at the tank wall. Let us note that because of microgravity, the bubbles that form at the surface by heterogeneous nucleations will not easily detach from the wall. One source of such detachments are vibrations. At the same time, another important mechanism was recently identified in the experiments conducted in the low gravity environment of the NASA's KC-135 aircraft [58–60]. In this mechanism, two bubbles have to be sufficiently close to each other, so that at a certain moment their coalescence occurs. The energy released in this process may be sufficient to break the resulting large bubble free from the wall [60]. Taking these two effects into account, we can write the following boundary condition for f_3 in Eq. (53):

$$\begin{aligned} -D\left.\frac{\partial f_3}{\partial z}\right|_{\text{wall}} &= k_1(R) f_2(R,\mathbf{r},t) \\ &+ \int_0^\infty \int_0^\infty k_2(R,R',R'') f_2(R',\mathbf{r},t) f_2(R'',\mathbf{r},t) dR' dR'', \end{aligned} \tag{54}$$

where k_1 and k_2 are the corresponding single and double bubble detachment rates, and f_2 is the distribution function of the bubbles attached to the tank wall. The latter, in turn, is governed by its own balance equation which contains growth terms and sink terms due to bubble departure:

$$\begin{aligned} \frac{\partial f_2}{\partial t} + \frac{\partial}{\partial R}\left(\frac{Q}{4\pi\rho_v q_L R^2} f_2\right) &= J\delta(R-R_0)\left(1 - A_0\int_0^\infty f_2(R,\mathbf{r},t)dR\right) \\ -k_1(R) f_2(R,\mathbf{r},t) - \int_0^\infty \int_0^\infty & k_2(R,R',R'') f_2(R',\mathbf{r},t) f_2(R'',\mathbf{r},t) dR' dR'', \end{aligned} \tag{55}$$

where J is the nucleation rate per unit area, which depends on the local temperature $T(\mathbf{r},t)$, A_0 is the area per nucleation site, and R_0 is the radius of newly nucleated bubbles. The first term in the right-hand side of Eq. (55) states that all empty nucleation sites will be activated with rate J.

5 Computational analysis

We now illustrate how the basic physics analysis discussed in the preceding sections can be supplemented by high-fidelity computational studies of the underlying fluid dynamics equations in order to obtain accurate information about the bubble dynamics. For definiteness, we consider the problem of vapor bubble collapse in subcooled LH2 upon bubble departure from a localized hot spot. To simplify matters, we assume that upon departure a spherical bubble is carried along with the flow of the subcooled liquid, where it shrinks uniformly by vapor condensation.

Let us begin with the governing equations for the liquid phase in the vicinity of the bubble. The motion of the liquid phase can be described by incompressible Navier-Stokes equation, written under the assumption of spherical symmetry [79]:

$$\frac{\partial u}{\partial r} + \frac{2u}{r} = 0, \quad \rho_L\left(\frac{\partial u}{\partial t} + u\frac{\partial u}{\partial r}\right) = -\frac{\partial p}{\partial r} + \mu_L\left(\frac{\partial^2 u}{\partial r^2} + \frac{2}{r}\frac{\partial u}{\partial r} - \frac{2u}{r^2}\right), \qquad r > R, \tag{56}$$

where r is the radial coordinate, $R = R(t)$ is the bubble radius, $u = u(r,t)$ is the radial liquid velocity for $r > R$, and $p = p(r,t)$ is the pressure inside the liquid. The liquid velocity u vanishes

at infinity. Similarly, the thermal diffusion equation in the liquid has the form [79]

$$c_L\rho_L\left(\frac{\partial T}{\partial t}+u\frac{\partial T}{\partial r}\right)=\kappa_L\left(\frac{\partial^2 T}{\partial r^2}+\frac{2}{r}\frac{\partial T}{\partial r}\right),\qquad r>R, \tag{57}$$

where $T=T(r,t)$ is the liquid temperature for $r>R$, and we neglected the heat generation due to viscous dissipation. From the conservation of mass, the corresponding boundary condition for the velocity u at $r=R$ are

$$j(t)=\rho_L(u(R+0,t)-\dot{R}(t)), \tag{58}$$

where j is the condensation mass flux at the bubble interface, and here and below the dot denotes time derivative.

Since the considered bubble dynamics is slow compared to the timescale of sound propagation in the vapor phase, with very good accuracy the pressure p_v inside the bubble is independent of space (a similar situation is realized in models of gaseous combustion [86]) and can be obtained from the condition of mechanical equilibrium at the interface:

$$p_v(t)=p(R,t)-2\mu_L\frac{\partial u(R+0,t)}{\partial r}+\frac{2\sigma_L}{R(t)}-j^2(t)(\rho_v^{-1}(R,t)-\rho_L^{-1}), \tag{59}$$

where the second term accounts for viscous forces [53], the third term is due to a pressure jump due to surface tension [53], and the fourth term is the recoil force due to evaporation/condensation flux [75,87]. With this assumption in mind, let us now turn to the governing equations for the gas phase. The conservation of vapor mass is described by [79]

$$\frac{\partial \rho_v}{\partial t}+\frac{\partial(\rho_v u)}{\partial r}+\frac{2\rho_v u}{r}=0,\qquad r<R, \tag{60}$$

where $\rho_v=\rho_v(r,t)$ is the vapor mass density and $u=u(r,t)$ is the radial vapor velocity for $r<R$. Furthermore, neglecting the contributions of the gas velocity and treating the vapor as an ideal gas, we can write the energy conservation in the form [79]

$$\frac{\partial(c_v\rho_v T)}{\partial t}+\frac{\partial(c_p\rho_v u T)}{\partial r}+\frac{2c_p\rho_v u T}{r}=\kappa_v\left(\frac{\partial^2 T}{\partial r^2}+\frac{2}{r}\frac{\partial T}{\partial r}\right),\qquad r<R, \tag{61}$$

where $T=T(r,t)$ is the vapor temperature for $r<R$ and c_v is the specific heat of vapor at constant volume. Note that the ideal gas equation of state used in Eq. (61):

$$p_v(t)=\rho_v(r,t)R_vT(r,t),\qquad r<R, \tag{62}$$

relates the vapor density ρ_v and temperature T at every point inside the bubble. The continuity of mass and energy at the interface read

$$j(t)=\rho_v(R,t)(u(R-0,t)-\dot{R}), \tag{63}$$

and

$$q_Lj(t)=\kappa_v\frac{\partial T(R-0,t)}{\partial r}-\kappa_L\frac{\partial T(R+0,t)}{\partial r},\qquad T(R-0,t)=T(R+0,t), \tag{64}$$

respectively. Finally, to close the obtained system of equations, we relate the condensation flux j with the conditions at the interface via the Hertz-Knudsen relation [88, 89], using a simplified equation for saturated vapor pressure p_s as a function of the temperature at the liquid-vapor interface [90]:

$$j(t) = \frac{p_v(t) - p_s(T(R,t))}{\sqrt{2\pi R_v T(R,t)}}, \qquad p_s(T) = p_c \left(\frac{T}{T_c}\right)^{\lambda}, \tag{65}$$

where $R_v = R_{H2}$, $p_c = 1.315 \times 10^6$ Pa and $T_c = 33.2$K are the critical pressure and temperature, respectively, and $\lambda = 5$ for hydrogen.

The continuity equation in both the gas and the liquid phase allows one to solve explicitly for the fluid velocity u at every point in space. For the liquid phase, which is incompressible, the solution is well-known:

$$u(r,t) = \frac{a(t)}{r^2}, \qquad r > R, \tag{66}$$

where $a(t)$ is some function of time only. Then, integrating Eq. (56) over r, with the help of Eq. (66) we obtain

$$p(R,t) = p_0 + \rho_L \left(\frac{\dot{a}}{R} - \frac{a^2}{2R^4}\right). \tag{67}$$

Also, substituting Eq. (66) into Eq. (57), we have

$$c_L \rho_L \left(\frac{\partial T}{\partial t} + \frac{a}{r^2}\frac{\partial T}{\partial r}\right) = \kappa_L \left(\frac{\partial^2 T}{\partial r^2} + \frac{2}{r}\frac{\partial T}{\partial r}\right), \qquad r > R. \tag{68}$$

In the gas phase, we can use the assumption that the vapor pressure p_v is space-independent to obtain a similar equation for u. Indeed, from Eqs. (60) and (62), we find that

$$\frac{\partial u}{\partial r} = \frac{1}{T}\frac{\partial T}{\partial t} + \frac{u}{T}\frac{\partial T}{\partial r} - \frac{\dot{p}_v}{p_v} - \frac{2u}{r}, \qquad r < R. \tag{69}$$

Substituting this expression into Eq. (61) and using Eq. (62) yields

$$c_p \rho_v \left(\frac{\partial T}{\partial t} + u\frac{\partial T}{\partial r}\right) = \kappa_v \left(\frac{\partial^2 T}{\partial r^2} + \frac{2}{r}\frac{\partial T}{\partial r}\right) + \dot{p}_v. \tag{70}$$

Now, let us use Eqs. (69) and (62) in Eq. (60), multiply the obtained equation by r^2 and integrate over r. After some algebra, we obtain a formula for u:

$$u(r,t) = \frac{1}{3\gamma p_v(t)} \left(3(\gamma - 1)\kappa_v \frac{\partial T(r,t)}{\partial r} - r\dot{p}_v(t)\right), \qquad r < R, \tag{71}$$

where $\gamma = c_p/c_v$. Combining Eq. (71) with (70) then yields

$$\frac{c_p p_v}{R_v T}\frac{\partial T}{\partial t} + \frac{\kappa_v}{T}\left(\frac{\partial T}{\partial r}\right)^2 - \frac{r\dot{p}_v}{3(\gamma-1)T}\frac{\partial T}{\partial r} = \kappa_v \left(\frac{\partial^2 T}{\partial r^2} + \frac{2}{r}\frac{\partial T}{\partial r}\right) + \dot{p}_v. \tag{72}$$

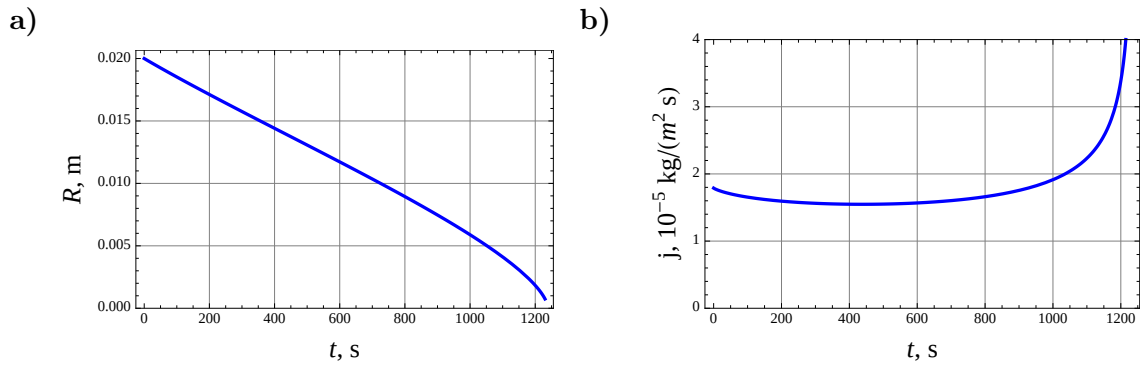

Figure 9. The dynamics of bubble collapse in the subcooled liquid obtained by solving the governing fluid dynamics equations: (a) the bubble radius R and (b) the condensation flux j, as functions of time.

We now substitute the obtained solutions for u into the boundary conditions at $r = R$. First of all, from Eqs. (58) and (66), we find that

$$\dot{R} = \frac{a}{R^2} - \frac{j}{\rho_L}. \tag{73}$$

On the other hand, from Eqs. (62), (63) and (71) we obtain

$$\dot{p}_v = \frac{3}{R}\left\{ j\left(\frac{\gamma p_v}{\rho_L} - (\gamma-1)c_p T(R,t)\right) - \frac{\gamma p_v a}{R^2} + (\gamma-1)\kappa_v \frac{\partial T(R,t)}{\partial r}\right\}, \tag{74}$$

where j is related to other variables via Eq. (65). Now, using Eq. (59) together with Eqs. (66) and (67), we also have

$$\dot{a} = \frac{a^2}{2R^3} + \frac{R}{\rho_L}\left\{ p_v - p_0 - \frac{4\mu_L a}{R^3} - \frac{2\sigma_L}{R} + j^2\left(\frac{(\gamma-1)c_p T(R,t)}{\gamma p_v} - \frac{1}{\rho_L}\right)\right\}. \tag{75}$$

This equation closes the system of equations describing $T(r,t)$, $R(t)$, $a(t)$ and $p_v(t)$. Thus, in order to obtain the full solution to the bubble dynamics, one needs to solve Eqs. (64), (65), (68), (72) – (75). For the problem of bubble collapse, the following initial conditions may be used:

$$R(0) = R_0, \quad p_v(0) = p_0, \quad a(0) = 0, \tag{76}$$

$$T(r,0) = T_{s0}, \quad r < R_0, \qquad T(r,0) = T_{L0} + \frac{(T_{s0} - T_{L0})R_0}{r}, \quad r > R_0. \tag{77}$$

The results of the numerical solution of the above equations under a simplifying assumption that $p_v(t) = p_s(T(R(t),t))$, justified in the considered situation [76], and with $R_0 = 2$ cm are presented in Fig. 9. As expected, the bubble shrinks to zero radius in finite time due to vapor condensation on the liquid-vapor interface. The heat released from the condensation is carried away into the subcooled liquid, and the temperature inside the bubble stays essentially constant, see Fig. 10. One can also see that the bubble collapse time is in very good agreement with the estimate obtained in Sec. 3.3.4.

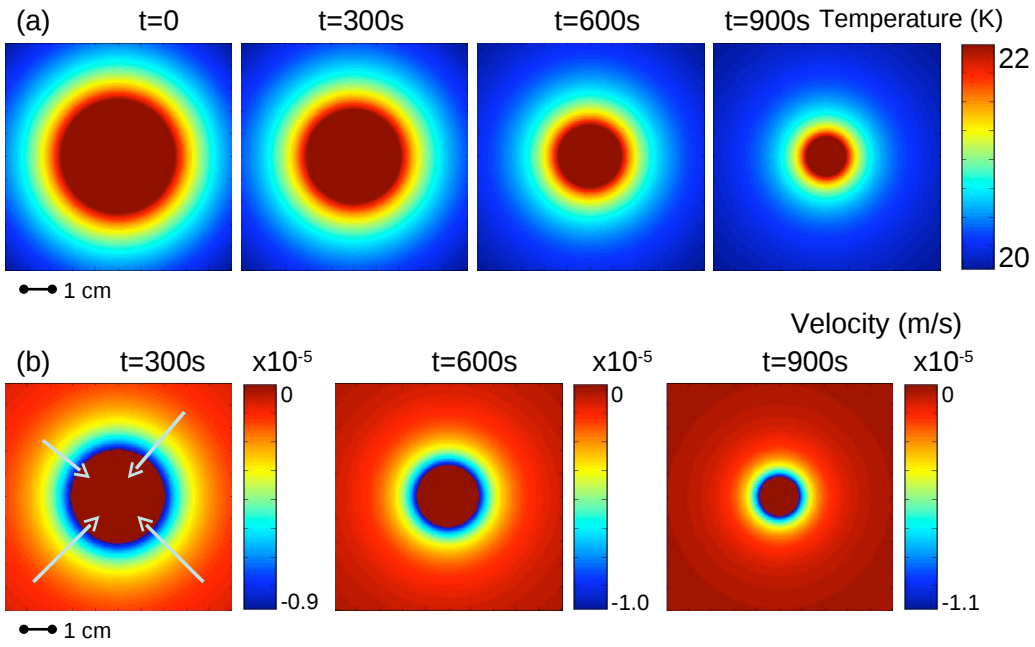

Figure 10. Temperature (a) and velocity (b) distributions in and around the collapsing bubble at times $t = 0, 300, 600, 900$ s.

6 Summary and conclusions

In conclusion, we have presented an overview of the physics-related issues associated with large-scale, long-term storage of LH2 in microgravity. A special difficulty associated with LH2 storage, as opposed to other cryogenic liquids, such as liquid oxygen or liquid methane, is its very low boiling point ($\sim$20K). Currently, no efficient cryocoolers exist that can operate at LH2 temperatures. This presently puts the promising ideas of ZBOT technologies out of reach in the case of LH2. For the same reason, other active cooling technologies, such as BAC, are also limited to the "tube-to-shield" concept, which can only partially address the problem of LH2 heat load reduction. Importantly, in the case of LH2 storage heat leaks through MLI penetration may become dominant challenges for enabling long-term storage in microgravity.

Below we first list the main physics-related issues of LH2 storage and then discuss potential challenges identified by our analysis.

In microgravity, the location, structure, and shape of the ullage space is generally unknown. The dominant forces determining the ullage bubble shape are capillary forces. The location of the ullage bubble is determined by a combination of the g-forces and the forces exerted on the ullage bubble by the liquid stirring flow. The ullage bubble may drift inside the tank due to the generally time-varying character of the g-forces.

Since the ullage bubble position is unknown and may be variable, boil-off vapor cannot be vented directly overboard. A combination of TVS and a fluid mixer may be used to control the boil-off pressure by maintaining the liquid in a subcooled state. This requires an addition of non-condensible cold pressurant gas to avoid ullage bubble collapse. Further heat load reduction strategies, both

active (BAC applied to an intermediate layer of the MLI) and passive (VCS utilizing the boil-off vapor from TVS to cool the MLI and penetrations) may also be necessary.

The stirring flow velocity of the liquid inside the tank is subject to competing constraints. Stirring has to be sufficiently strong to ensure efficient heat transfer from the tank walls through the liquid into the TVS heat exchanger. Stirring has to be sufficiently weak to avoid deforming or breaking the ullage bubble. Excessive stirring may result in the injection of unwanted energy into the liquid.

Ullage motion driven by a strong stirring flow may result in a TVS hazard, whereby the ullage bubble may be captured by the TVS intake and block normal operation of TVS. As a consequence, TVS may fail to control the tank pressure, or bubbles filled with non-condensible pressurant gas may come out of the TVS recirculation outlet.

This implementation faces a number of challenges related to fundamental physics.

1. On the basis of correlations derived under earth gravity, it is conceivable that both natural convection in microgravity and stirring may keep the tank wall temperature below the saturation point away from the possible temperature hot-spots due to localized heat leaks through MLI penetrations. Efficient heat removal from the penetrations may require highly conductive tank wall material of sufficient thickness and vapor cooling. On-orbit experiments and further physics-based modeling is necessary to establish new reliable correlations which are needed to design a proper strategy for tank temperature control.

2. Unpredictable changes of the flow conditions may result in overheating of the liquid near the tank wall. For high wall conductivities this may lead to the explosive boiling hazard, whereby a large mass of liquid becomes superheated in a rather large area around a temperature hot-spot on the tank wall or near flow stagnation points after a long delay time. The ensuing fast nucleate boiling may create a pressure jump and a strong liquid flow affecting the ullage bubble.

3. Single large vapor bubbles attached to the tank walls or many small bubbles injected into the liquid may form at the points of strong localized heat leaks. The choice of the scenario depends sensitively on the mechanism of bubble departure from the tank wall during nucleate boiling near hot-spots. Key factors determining this mechanism are the liquid contact angle, the tank surface properties, microgravity magnitude and direction, g-jitter, Ostwald ripening and bubble merging.

4. The bubbles inside the liquid may drift with the stirring flow and accumulate in its stagnation areas, resulting in the formation of complex multi-phase liquid-vapor foam-like structures. The foam may further thermally insulate parts of the tank wall from the subcooled liquid, increasing the boiling rate in those regions. The associated pressure increase cannot be well controlled by TVS.

5. Boil-off bubbles may not be easy to remove by an overpressurization, since the collapsing bubbles release heat into the surrounding liquid and raise its temperature to saturation. In the presence of TVS hazard by the ullage motion, overpressurization may be ineffective in the presence of non-condensible pressurant gas inside the vapor bubbles.

6. The multi-phase liquid-vapor foam may grow at the expense of shrinking of the ullage bubble, when the vapor mass is transferred from the ullage into the foam. This phenomenon is

complicated by the pressurant gas dissolution hazard, which is further amplified by strong stirring. The dissolved non-condensible pressurant gas may enter into the vapor bubbles of the foam. As a result, these bubbles may be difficult or impossible to eliminate by applying overpressurization.

References

1. G. P. Sutton and O. Biblarz. *Rocket Propulsion Elements*. John Wiley and Sons, Inc., Hoboken, NJ, 2001.

2. D. J. Chato. Cryogenic fluid transfer for exploration. *Cryogenics*, 48:206–209, 2008.

3. D. Plachta and P. Kittel. An updated zero boil-off cryogenic propellant storage analysis applied to upper stages or depots in an LEO environment. Technical Report TM—2003-211691, NASA, 2003.

4. B. F. Kutter, F. Zegler, G. O'Neil, and B. Pitchford. A practical, affordable cryogenic propellant depot based on ULA's flight experience. In *AIAA SPACE 2008 Conference and Exposition*, 2008.

5. J. A. Goff, B. F. Kutter, F. Zegler, D. Bienhoff, F. Chandler, and J. Marchetta. Realistic near-term propellant depots: Implementation of a critical spacefaring capability. In *AIAA SPACE 2009 Conference and Exposition*, 2009.

6. S. M. Motil, M. L. Meyer, and S. P. Tucker. Cryogenic fluid management technologies for advanced green propulsion systems. Technical Report TM-2007-214810, NASA, 2007.

7. L. J. Salerno and P. Kittel. Cryogenics and the human exploration of Mars. *Cryogenics*, 39:381–388, 1999.

8. R. F. Lacovic, F. C. Yeh, S. V. Szabo, R. J. Brun, A. J. Stofan, and J. A. Berns. Management of cryogenic propellants in a full-scale orbiting space vehicle. Technical Report TN D-4571, NASA, 1968.

9. D. Glover. NASA cryogenic fluid management space experiment efforts 1960-1990. Technical Report TM-103752, NASA, 1991.

10. F. T. Dodge. *The New "Dynamic Behavior of Liquids in Moving Containers"*. Southwest Research Institute, San Antonio, TX, 2000.

11. D. J. Chato. Low gravity issues of cryogenic fluid management technologies enabling exploration, 2009.

12. M. P. Doherty, J. D. Gaby, L. J. Salerno, and S. G. Sutherlin. Cryogenic fluid management technology for moon and mars missions. Technical Report TM-2010-216070, NASA, 2010.

13. M. Donabedian, editor. *Spacecraft thermal control handbook. Volume 2, Cryogenics*. The Aerospace Press, El Segundo, CA, 2003.

14. D. J. Chato. The role of flight experiments in the development of cryogenic fluid management technologies. *Cryogenics*, 46:82–88, 2006.

15. NASA Technical Report HSM-R421-67. *Evaluation of AS-203 Low Gravity Orbital Experiment*, 1967.

16. NASA-TM-X-881. *Apollo Systems Description. Volume II. Saturn Launch Vehicles*, 1964.

17. V. K. Dhir. Mechanistic prediction of nucleate boiling heat transfer–achievable or a hopeless task? *J. Heat Transfer*, 128:1–12, 2006.

18. E. I. Nesis. Boiling of liquids. *Sov. Phys. – Uspekhi*, 8:883–907, 1965.

19. C. E. Brennen. *Fundamentals of Multiphase Flows*. Cambridge University Press, 2005.

20. N. I. Kolev. *Multiphase flow dynamics*, volume 2. Springer-Verlag, Berlin, 2nd edition, 2005.

21. V. K. Dhir. Boiling under microgravity conditions. In *Proceedings of 12th International Heat Transfer Conference*, Grenoble, France, 2002.

22. J. Kim. Review of reduced gravity boiling heat transfer: US research. *J. Jpn. Soc. Microgravity Appl.*, 20:264–271, 2003.

23. NASA's Exploration System Architecture Study (Final Report). NASA-TM-2005-214062, 2005.

24. E. M. Lifshits and L. P. Pitaevskii. *Course of Theoretical Physics*, volume 8. Pergamon Press, London, 1980.

25. NASA-TM-X-68725. *Apollo Program Summary Report*, 1975.

26. NASA-TM-X-69534. *Saturn V Launch Vehicle Flight Evaluation Report – AS-512. Apollo 17 Mission*, 1973.

27. R. W. Orloff. Apollo by the numbers: A statistical reference. Technical report, NASA SP-2000-4029, 2000.

28. C. W. Keller, G. R. Cunnington, and A. P. Glassford. Thermal performance of multilayer insulations. Technical Report CR-134477, NASA, 1974.

29. J. R. Feller. Some simple calculations to assess the effectiveness of passive and active boil-off reduction techniques to EDS. NASA-ARC Cryogenics Group, 2009.

30. L.J. Hastings, D.W. Plachta, L. Salerno, and P. Kittel. An overview of NASA efforts on zero boiloff storage of cryogenic propellants. *Cryogenics*, 41:833–839, 2002.

31. M. E. Moran. Cryogenic fluid storage technology development: Recent and planned efforts at NASA. Technical Report TM—2009-215514, NASA, 2009.

32. C. Panzarella, D. Plachta, and M. Kassemi. Pressure control of large cryogenic tanks in microgravity. *Cryogenics*, 44:475–483, 2004.

33. J. Feller, L. Salerno, A. Kashani, J. Maddocks, B. Helvensteijn, G. Nellis, and Y. Gianchandani. Distributed cooling techniques for cryogenic boil-off reduction systems. In *The Proceedings of the 15th International Cryocooler Conference*, 2008.

34. E. R. Canavan, R. F. Boyle, and S. Mustafi. Active costorage of cryogenic propellants for exploration. In Mohamed S. El-Genk, editor, *Space Technology and Applications International Forum–STAIF 2008*, volume 969, pages 733–740. AIP, 2008.

35. J. F. LeBar and E. C. Cady. The advanced cryogenic evolved stage (ACES) – a low-cost, low-risk approach to space exploration launch. In *AIAA 2006-7454*, 2006.

36. K. R. Hanby. *Handbook on Materials for Superconducting Machinery*. Battelle Columbus Labs, Ohio Metals and Ceramics Information Center, Columbus, OH, 1974.

37. M. P. Malkov. *A reference on physics and engineering fundamentals of cryogenics (in Russian)*. Energatomizdat, Moscow, 1985.

38. A. Woodcraft. Predicting the thermal conductivity of aluminium alloys in the cryogenic to room temperature range. *Cryogenics*, 45:421–432, 2005.

39. R.D. McCarty, J. Hord, and H.M. Roder. *Selected properties of hydrogen (engineering design data)*, volume 168 of *Natl. Bur. Stand. Monographs*. National Bureau of Standards, 1981.

40. M. M. Hasan, C. S. Lin, R. H. Knoll, and M. D. Bentz. Tank pressure control experiment: Thermal phenomena in microgravity. Technical Report TP-3564, NASA, 1996.

41. L. Bewilogua, R. Knoner, and G. Wolf. Heat transfer in boiling hydrogen neon nitrogen and argon. *Cryogenics*, 6:36–39, 1966.

42. Y. A. Kirichenko, K. V. Rusanov, and E. G. Tyurina. Heat-transfer in subcooled liquid cryogens. *Cryogenics*, 23:209–211, 1983.

43. L. Bewilogua, R. Knöner, and H. Vinzelberg. Heat transfer in cryogenic liquids under pressure. *Cryogenics*, 15:121–125, 1975.

44. F. P. Incopera and D. P. DeWitt. *Fundamentals of Heat and Mass Transfer*. John Wiley and Sons, Inc., New York, 2007.

45. J. R. Feller, D. W. Plachta, G. Mills, and C. McLean. Demonstration of a cryogenic boil-off reduction system employing an actively cooled thermal radiation shield. Technical report, NASA, 2010.

46. F. W. Schmidt, R. E. Henderson, and C. H. Wolgemuth. *Introduction to Thermal Sciences*. John Wiley and Sons, Inc., 1993.

47. V. L. Streeter, E. B. Wylie, and K. W. Bedford. *Fluid Mechanics*. McGraw-Hill, 1998.

48. S. E. Haaland. Simple and explicit formulas for the friction factor in turbulent flow. *J. Fluids Eng.*, 102:89–90, 1983.

49. P.J. Linstrom and W.G. Mallard, editors. *Thermophysical Properties of Fluid Systems*. NIST Chemistry WebBook, NIST Standard Reference Database Number 69. National Institute of Standards and Technology, Gaithersburg MD, 2010.

50. W. B. Streett, R. E. Sonntag, and G. J. Van Wylen. Liquid—vapor equilibrium in the system normal hydrogen—helium. *The Journal of Chemical Physics*, 40:1390–1395, 1964.

51. G. Cini-Castagnoli, A. Giardini-Guidoni, and F. P. Ricci. Diffusion of neon, ht, and deuterium in liquid hydrogen. *Phys. Rev.*, 123:404–406, 1961.

52. W. P. A. Hass, G. Seidel, and N. J. Poulis. Nuclear spin relaxation and molecular diffusion in liquid hydrogen. *Physica*, 26:834 – 852, 1960.

53. R. Clift, J. R. Grace, and M. E. Weber. *Bubbles, Drops, and Particles*. Academic Press, New York, 1978.

54. R. Marek and J. Straub. The origin of thermocapillary convection in subcooled nucleate pool boiling. *Int. J. Heat Mass Transfer*, 44:619 – 632, 2001.

55. M. Barthes, C. Reynard, R. Santini, and L. Tadrist. Non-condensable gas influence on the marangoni convection during a single vapour bubble growth in a subcooled liquid. *Europhys. Lett.*, 77:14001, 2007.

56. R. H. Flachbart, L. J. Hastings, A. Hedayat, S. L. Nelson, and S. Tucker. Testing the effect of helium pressurant on thermodynamic vent system performance with liquid hydrogen. In J. G. Weisend II, editor, *CP985, Advances in Cryogenic Engineering: Transactions of the Cryogenic Engineering Conference — CEC*, volume 53, 2008.

57. S. H. Ho and M. M. Rahman. Three-dimensional analysis for liquid hydrogen in a cryogenic storage tank with heat pipe-pump system. *Cryogenics*, 48:31–41, 2008.

58. J. Kim, J. F. Benton, and D. Wisniewski. Pool boiling heat transfer on small heaters: effect of gravity and subcooling. *Int. J. Heat Mass Transfer*, 45:3919–3932, 2002.

59. C. D. Henry and J. Kim. A study of the effects of heater size, subcooling, and gravity level on pool boiling heat transfer. *Int. J. Heat Fluid Flow*, 25:262–273, 2004.

60. UCLA Heat Transfer Lab. Nucleate boiling in the low gravity environment of the KC-135 aircraft. http://boiling.seas.ucla.edu/multimedia_gallery.htm, 2009.

61. Y. A. Kirichenko, L. A. Slobozhanin, and N. S. Shcherbakova. Analysis of quasi-static conditions of boiling onset and bubble departure. *Cryogenics*, 23:110–112, 1983.

62. W. B. Bald. Bubble-growth constants for liquid-hydrogen and liquid-helium. *Cryogenics*, 16:709–712, 1976.

63. A. Mukherjee and V. K. Dhir. Study of lateral merger of vapor bubbles during nucleate pool boiling. *Journal of Heat Transfer*, 126:1023–1039, 2004.

64. S. Siedel, S. Cioulachtjian, and J. Bonjour. Experimental analysis of bubble growth, departure and interactions during pool boiling on artificial nucleation sites. *Exp. Therm. Fluid. Sci.*, 32:1504–1511, 2008.

65. G. M. Zlobintsev, V. V. Kozinets, B. A. Merisov, E. M. Ogneva, V. I. Sokolov, and A. V. Blinova. Thermal conductivity of structural aluminum alloys at low temperatures. *Metal Sci. and Heat Treat.*, 17:436–437, 1975.

66. J. Straub. Boiling heat transfer and bubble dynamics in microgravity. In J. P. Hartnett, editor, *Advances in Heat Transfer*, volume 35. Academic Press, San Diego, CA, 2001.

67. M.-C. Duluc, B. Stutz, and M. Lallemand. Boiling incipience in liquid nitrogen induced by a step change in heat flux. *Int. J. Heat Mass Transfer*, 51:1738 – 1750, 2008.

68. M. E. Bland, C. A. Bailey, and G. Davey. Boiling from metal-surfaces immersed in liquid-nitrogen and liquid-hydrogen. *Cryogenics*, 13:651–657, 1973.

69. J. Li and G. P. Petersen. Microscale heterogeneous boiling on smooth surfaces—from bubble nucleation to bubble dynamics. *Int. J. Heat Mass Transfer*, 48:4316–4332, 2005.

70. J. Kim. Review of nucleate pool boiling bubble heat transfer mechanisms. *Int. J. Multiphase Flow*, 35:1067–1076, 2009.

71. M. S. Plesset and S. A. Zwick. The growth of vapor bubbles in superheated liquids. *J. Appl. Phys.*, 25:493–500, 1954.

72. L. E. Scriven. On the dynamics of phase growth. *Chem. Eng. Sci.*, 10:1–13, 1959.

73. V. S. Nikolayev, D. A. Beysens, G. L. Lagier, and J. Hegseth. Growth of a dry spot under a vapor bubble at high heat flux and high pressure. *International Journal of Heat and Mass Transfer*, 44:3499 – 3511, 2001.

74. V. Nikolayev, D. Beysens, Y. Garrabos, C. Lecoutre, and D. Chatain. Bubble spreading during the boiling crisis: modelling and experimenting in microgravity. *Microgravity Sci. Technol.*, 18:34–37, 2006.

75. V. S. Nikolayev. Dynamics of the triple contact line on the non-isothermal heater. *Phys. Fluids*, 22:082105, 2010.

76. V. V. Osipov and C. B. Muratov. Dynamic condensation blocking in cryogenic refueling. *Appl. Phys. Lett.*, 93:224105, 2008.

77. M. Přibyl, C. B. Muratov, and S. Y. Shvartsman. Discrete models of autocrine cell communication in epithelial layers. *Biophys. J.*, 84:3624–3635, 2003.

78. Y. Abe and A. Iwasaki. Microgravity experiments on dual vapor bubbles of self-wetting fluid. *AIP Conf. Proc.*, 608:189–196, 2002.

79. L. D. Landau and E. M. Lifshits. *Course of Theoretical Physics*, volume 6. Pergamon Press, London, 1987.

80. L. D. Landau and E. M. Lifshits. *Course of Theoretical Physics*, volume 8. Pergamon Press, London, 1984.

81. V. A. Marchenko and E. Ya. Khruslov. *Homogenization of partial differential equations*, volume 46 of *Progress in Mathematical Physics*. Birkhäuser, Boston, MA, 2006.

82. C. B. Muratov and S. Y. Shvartsman. Boundary homogenization for periodic arrays of absorbers. *Multiscale Model. Simul.*, 7:44–61, 2008.

83. G. C. Papanicolaou and S. R. S. Varadhan. Diffusion in regions with many small holes. In *Stochastic differential systems (Proc. IFIP-WG 7/1 Working Conf., Vilnius, 1978)*, volume 25 of *Lecture Notes in Control and Information Sci.*, pages 190–206. Springer, Berlin, 1980.

84. L. D. Landau and E. M. Lifshits. *Course of Theoretical Physics*, volume 5. Pergamon Press, London, 1980.

85. E. M. Lifshits and L. P. Pitaevskii. *Physical kinetics*. Pergamon Press, Oxford, 1981.

86. F. A. Williams. *Combustion Theory*. The Benjamin/Cummings Publishing Company, Inc., Menlo Park, CA, 1985.

87. Andrea Prosperetti and M. S. Plesset. The stability of an evaporating liquid surface. *Physics of Fluids*, 27:1590–1602, 1984.

88. Y.-P. Pao. Application of kinetic theory to problem of evaporation and condensation. *Phys. Fluids*, 14:306–312, 1971.

89. L. D. Koffman, M. S. Plesset, and L. Lees. Theory of condensation and evaporation. *Phys. Fluids*, 27:876–880, 1984.

90. J. A. Clark. Universal equations for saturation vapor pressure. In *IAA/ASME/SAE/ASEE Joint Propulsion Conference and Exhibit, AIAA 2004-4088*, 2004.

91. L. C. Evans. *Partial Differential Equations*, volume 19 of *Graduate Studies in Mathematics*. American Mathematical Society, Providence, RI, 1998.

92. M. Abramowitz and I. Stegun, editors. *Handbook of mathematical functions*. National Bureau of Standards, 1964.

93. C. B. Muratov. Droplet phases in non-local Ginzburg-Landau models with Coulomb repulsion in two dimensions. *Comm. Math. Phys.*, 299:45–87, 2010.

Appendix A

Analysis of heat exchange between the cooling tube and the strut

Here we derive a set of approximate differential equations that describe the distribution of temperature in a tubular strut of material with thermal conductivity $\kappa_{\rm strut}$, radius $R_{\rm strut}$, thickness $d_{\rm strut}$, and length $L_{\rm strut}$, with a helical coil made of a GH2-carrying tube wound around (see Fig. 2). The pitch of the tube helix is denoted by $d_{\rm tube}$ and is assumed to be much smaller than $R_{\rm strut}$. Let $x > 0$ be the coordinate along the strut and let $x = 0$ correspond to the point of the strut attachment to the tank wall. Consider the heat balance in the strut on the interval $[x_0 - \frac{1}{2}d_{\rm tube}, x_0 + \frac{1}{2}d_{\rm tube}]$. Assuming that the strut temperature $T(x)$ varies appreciably only in the x-direction, to a first approximation the steady heat balance reads

$$2\pi R_{\rm strut} d_{\rm strut} \kappa_{\rm strut} \left.\frac{dT}{dx}\right|_{x=x_0-\frac{1}{2}d_{\rm tube}}^{x=x_0+\frac{1}{2}d_{\rm tube}} = 4\pi^2 R_{\rm strut} R_{\rm tube} h_{\rm tube} (T(x_0) - T_v(x_0)), \tag{A78}$$

where $T_v(x)$ is the vapor temperature at position x along the strut in the tube, $h_{\rm tube}$ is the heat transfer coefficient obtained in Eq. (12), and we assumed that the tube is in perfect thermal contact with the strut. Using Eq. (11) to express $h_{\rm tube}$ in terms of the tube Nusselt number and approximating the jump in the derivative of the temperature above by $d_{\rm tube} d^2T/dx^2$ evaluated at $x = x_0$, after some algebra we obtain the following differential equation for $T(x)$:

$$l_{\rm strut}^2 \frac{d^2T}{dx^2} = T - T_v, \qquad l_{\rm strut} = \sqrt{\frac{\kappa_{\rm strut} d_{\rm strut} d_{\rm tube}}{\pi \kappa_v {\rm Nu}_{\rm tube}}} \tag{A79}$$

with boundary conditions

$$\left.\frac{dT}{dx}\right|_{x=0} = 0, \qquad T\Big|_{x=L_{\rm strut}} = T_0, \tag{A80}$$

where we took into account that all the heat from the strut is captured by the tube and thus does not enter into the tank at $x = 0$, and that the strut is thermalized with the environment at $x = L_{\rm strut}$. Note that the parameter $l_{\rm strut}$ has the dimension of length and characterizes the length scale at which the strut temperature would equilibrate to the tube temperature, if the latter were kept constant. For the parameters of Sec. 3.1.5, we find $l_{\rm strut} \simeq 2.5$ cm.

On the other hand, the heat balance for GH2 in the interval $[x_0 - \frac{1}{2}d_{\rm tube}, x_0 + \frac{1}{2}d_{\rm tube}]$ reads

$$c_p J_{\rm strut} T_v(x) \Big|_{x=x_0-\frac{1}{2}d_{\rm tube}}^{x=x_0+\frac{1}{2}d_{\rm tube}} = 4\pi^2 R_{\rm strut} R_{\rm tube} h_{\rm tube} (T(x_0) - T_v(x_0)). \tag{A81}$$

Once again, approximating the jump in $T_v(x)$ by $d_{\rm tube} dT_v/dx$ at $x = x_0$, we can write this as a differential equation

$$c_p J_{\rm strut} d_{\rm tube} \frac{dT_v}{dx} = 4\pi^2 R_{\rm strut} R_{\rm tube} h_{\rm tube} (T(x_0) - T_v(x_0)). \tag{A82}$$

Then using Eq. (A78) and integrating the obtained equation, we get

$$T_v = T_{L0} + l_v \frac{dT}{dx}, \qquad l_v = \frac{2\pi R_{\rm strut} d_{\rm strut} \kappa_{\rm strut}}{c_p J_{\rm strut}}, \tag{A83}$$

where we took into account that GH2 enters with $T_v = T_{L0}$ at $x = 0$. Here the parameter l_v also has a dimension of length and characterizes the length scale on which the vapor temperature approaches that of the strut, if the latter follows that of the vapor (when cooling is efficient). For the parameters of Sec. 3.1.5, we find $l_v \simeq 10$ cm.

Finally, substituting Eq. (A83) into (A79), we obtain a single linear equation

$$l_{\rm strut}^2 \frac{d^2T}{dx^2} + l_v \frac{dT}{dx} - T + T_{L0} = 0. \tag{A84}$$

Together with the boundary conditions in Eq. (A80) this simple boundary value problem admits an exact solution, which is too cumbersome to be written down as an explicit formula. We omit the final answer, which is plotted in Fig. 3 for various parameters.

Appendix B

Analysis of heat spreading in the tank wall

Consider a flat infinite layer of aluminum of thickness h, to which heat power P is injected uniformly into a disk of radius $r_0 \gtrsim h$ at one of the surfaces. Averaging the heat conductance equation written in cylindrical coordinates over the film thickness, we obtain an equation

$$c_w \rho_w \frac{\partial T}{\partial t} = \frac{\kappa_w}{r} \frac{\partial}{\partial r} \left(r \frac{\partial T}{\partial r} \right) + \frac{P}{\pi r_0^2 h} H(r_0 - r), \tag{B85}$$

where $H(x)$ is the Heaviside function. The solution $T(r,t)$ of this equation with initial condition $T(r,0) = T_{L0}$ can be written in terms of the two-dimensional heat kernel (see e.g. [91]). From that solution, we find that the maximum temperature, which is equal to the value of $T(0,t)$ is

$$\begin{aligned} T_{max}(t) &= T_{L0} + \frac{P}{2\pi r_0^2 h \kappa_w} \int_0^t \frac{dt'}{t-t'} \int_0^{r_0} r dr \, \exp(-c_w \rho_w r^2/(4\kappa_w (t-t'))) \\ &= T_{L0} + \frac{P}{4\pi c_w \rho_w \kappa_w h r_0^2} \left[4t\kappa_w \left(1 - e^{-\frac{c_w \rho_w r_0^2}{4\kappa_w t}} \right) + c_w \rho_w r_0^2 \Gamma \left(0, \frac{c_w \rho_w r_0^2}{4\kappa_w t} \right) \right] \\ &= T_{L0} + \frac{P}{4\pi h \kappa_w} \ln \left(\frac{4\kappa_w t}{e^{\gamma - 1} c_w \rho_w r_0^2} \right) + O(t^{-1}), \end{aligned} \tag{B86}$$

where $\Gamma(a,z)$ is the incomplete Gamma-function and $\gamma \simeq 0.5772$ is the Euler constant [92]. Approximating the solution in the tank wall by Eq. (B86) and evaluating the coefficient inside the logarithm numerically, we obtain the estimate in Eq. (16).

Appendix C

Effect of heat loss into the liquid on the heat conduction in the tank wall

Consider an infinite layer of aluminum of thickness h injected with a heat leak P uniformly through a disk of radius $r_0 \gtrsim h$, as in Appendix B, in contact with a layer of liquid of thickness R_0 undergoing free convection. If Nu_{R_0} is the Nusselt number associated with convection and $\kappa_L \mathrm{Nu}_{R_0}/R_0$ is the corresponding heat transfer coefficient, then the equation of heat conductance in the layer, averaged over the layer thickness (see e.g. [77, Appendix] for a similar treatment) and written in polar coordinates is

$$c_w \rho_w \frac{\partial T}{\partial t} = \frac{\kappa_w}{r} \frac{\partial}{\partial r} \left(r \frac{\partial T}{\partial r} \right) - \frac{\kappa_L \mathrm{Nu}_{R_0} (T - T_{L0})}{h R_0} + \frac{P}{\pi r_0^2 h} H(r_0 - r). \tag{C87}$$

In contrast to Eq. (B85), this equation admits steady state solutions as $t \to \infty$, due to the screening effect of the heat loss, characterized by the screening length given by Eq. (17) (similar equations arise in the studies of Debye-Hückel theory of electrolytes, in which l_s is the Debye radius [84]). Indeed, the stationary solution of Eq. (C87) is [93, Eq. (3.39)]:

$$T(r) = T_{L0} + \frac{P}{\pi r_0^2 \kappa_w h} \times \begin{cases} l_s^2 - r_0 l_s K_1(r_0/l_s) I_0(r/l_s), & r \le r_0, \\ r_0 l_s I_1(r_0/l_s) K_0(r/l_s), & r \ge r_0, \end{cases} \tag{C88}$$

where $I_n(x)$ and $K_n(x)$ is the modified Bessel functions of order n of the first and second kind, respectively [92], and so the solution decays exponentially at lengths of order l_s. The maximum of $T(r)$ is achieved at $r = 0$, and we have

$$\max T(r) = T_{L0} + \frac{P}{2\pi \kappa_w h} \left[\ln \left(\frac{2 \exp\left(\frac{1}{2} - \gamma\right) l_s}{r_0} \right) + O\left(\frac{r_0^2}{l_s^2} \ln \frac{l_s}{r_0} \right) \right], \tag{C89}$$

where $\gamma \simeq 0.5772$ is the Euler constant [92]. Evaluating the numerical factor inside the logarithm and dropping higher order terms, we obtain Eq. (18).

Appendix D

Spreading of heat from the wall into the liquid

Consider a flat infinite layer of aluminum at $z = 0$ covered by a semi-infinite layer of LH2 at $z > 0$. The steady heat equation for aluminum averaged over the layer thickness reads

$$\kappa_w \left(\frac{\partial^2 T}{\partial x^2} + \frac{\partial^2 T}{\partial y^2} \right) + \frac{\kappa_L}{h} \left. \frac{\partial T}{\partial z} \right|_{z=+0} + \frac{P}{\pi r_0^2 h} H\left(r_0 - \sqrt{x^2 + y^2} \right) = 0, \tag{D90}$$

where the last term is as before and the boundary term comes from the continuity of heat flux from LH2 into aluminum. The corresponding heat conductance problem for LH2 is given by the following boundary value problem:

$$\frac{\partial^2 T}{\partial x^2} + \frac{\partial^2 T}{\partial y^2} + \frac{\partial^2 T}{\partial z^2} = 0, \qquad z > 0, \tag{D91}$$

and continuity of T is assumed down to $z = 0$. Applying Fourier Transform in the x and y variables to Eq. (D91):

$$\hat{T}_{\mathbf{q}}(z) = \int_{-\infty}^{+\infty} \int_{-\infty}^{+\infty} e^{iq_1 x + iq_2 y} \left(T(x, y, z) - T_{L0}\right) dx\, dy, \tag{D92}$$

where $\mathbf{q} = (q_1, q_2)$, and solving the obtained equation, we get

$$\hat{T}_{\mathbf{q}}(z) = \hat{T}_{\mathbf{q}}(0) e^{-qz}, \qquad q = \sqrt{q_1^2 + q_2^2}. \tag{D93}$$

In particular, the Fourier Transform of the Dirichlet-to-Neumann map associated with (D91) is

$$\left.\frac{\partial \hat{T}_{\mathbf{q}}}{\partial z}\right|_{z=+0} = -q \hat{T}_{\mathbf{q}}(0). \tag{D94}$$

Plugging this expression into the Fourier-transformed Eq. (D90) and using the expression of [93, Eq. (B6)] for the transform of the characteristic function of a disk, after some algebra we obtain

$$\hat{T}_{\mathbf{q}}(0) = \frac{2P J_1(q r_0)}{r_0 \kappa_L q^2 (Lq + 1)}, \tag{D95}$$

where $J_n(x)$ is the Bessel function of the first kind of order n, and we used Eq. (20). Inverting the Fourier transform in Eq. (D95) and performing the integrations, after some algebra we find $\max T(x, y, z) = T(0, 0, 0)$, with

$$\max T = T_{L0} + \frac{P}{2\kappa_L r_0} \left[H_1\left(\frac{r_0}{L}\right) - Y_1\left(\frac{r_0}{L}\right) - \frac{2L}{\pi r_0} \right], \tag{D96}$$

where $H_1(z)$ and $Y_1(z)$ are the Struve function and the modified Bessel function of the second kind, respectively [92]. Finally, expanding the expression in Eq. (D96) in a series in r_0, we find that

$$\max T = T_{L0} + \frac{P}{2\pi \kappa_w h} \left[\ln\left(\frac{2\exp(\frac{1}{2} - \gamma) L}{r_0} \right) + O\left(\frac{r_0^2}{L^2} \ln \frac{L}{r_0} \right) \right], \tag{D97}$$

which coincides with Eq. (C89) with l_s replaced with L, to the leading order.

Appendix E

Bubble collapse in the subcooled liquid via conduction through thermal boundary layer

Consider a bubble of radius $R(t)$, whose interface is at saturation temperature T_{s0} suspended in a subcooled liquid with temperature T_{L0}. In the thermal boundary layer approximation the heat conduction near the interface may be approximated by a one-dimensional initial boundary value problem for the liquid temperature $T(r, t)$

$$c_L \rho_L \frac{\partial T}{\partial t} = \kappa_L \frac{\partial^2 T}{\partial r^2}, \qquad T(R, t) = T_{s0},\ T(\infty, t) = T_{L0}, \qquad T(r, 0) = T_{L0}. \tag{E98}$$

The solution of this problem is

$$T(r,t) = T_{L0} + (T_{s0} - T_{L0}) \operatorname{erf}\left(\sqrt{\frac{c_L \rho_L (r-R)^2}{4\kappa_L t}}\right), \tag{E99}$$

where $\operatorname{erf}(z)$ is the error function [92]. From this formula, we find that the heat flux through the interface is

$$q(t) = -\kappa_L \frac{\partial T(R,t)}{\partial r} = \sqrt{\frac{c_L \rho_L \kappa_L (T_{s0} - T_{L0})^2}{\pi t}}. \tag{E100}$$

The substituting this expression to the heat balance equation $4\pi R^2 dR \rho_v q_L = -4\pi R^2 q(t) dt$, whose solution is given by Eq. (26).

REPORT DOCUMENTATION PAGE

Form Approved
OMB No. 0704–0188

1. REPORT DATE *(DD-MM-YYYY)*	2. REPORT TYPE	3. DATES COVERED *(From - To)*
01-10-2011	Technical Memorandum	

4. TITLE AND SUBTITLE
Issues of Long-Term Cryogenic Propellant Storage in Microgravity

5a. CONTRACT NUMBER

5b. GRANT NUMBER

5c. PROGRAM ELEMENT NUMBER

6. AUTHOR(S)
V. B. Muratov, V. V. Osipov and V. N. Smelyanskiy

5d. PROJECT NUMBER

5e. TASK NUMBER

5f. WORK UNIT NUMBER

7. PERFORMING ORGANIZATION NAME(S) AND ADDRESS(ES)
NASA NASA Ames Research Center Moffett Field, CA 94035-1000

8. PERFORMING ORGANIZATION REPORT NUMBER
L–

9. SPONSORING/MONITORING AGENCY NAME(S) AND ADDRESS(ES)
National Aeronautics and Space Administration
Washington, DC 20546-0001

10. SPONSOR/MONITOR'S ACRONYM(S)
NASA

11. SPONSOR/MONITOR'S REPORT NUMBER(S)
NASA/TM–2011–215988

12. DISTRIBUTION/AVAILABILITY STATEMENT
Unclassified-Unlimited
Subject Category
Availability: NASA CASI (443) 757-5802

13. SUPPLEMENTARY NOTES
An electronic version can be found at http://ntrs.nasa.gov.

14. ABSTRACT

Modern multi-layer insulation (MLI) allows to sharply reduce the heat leak into cryogenic propellant storage tanks through the tank surface and, as a consequence, significantly extend the storage duration. In this situation the MLI penetrations, such as support struts, feed lines, etc., become one of the most significant challenges of the tank's heat management. This problem is especially acute for liquid hydrogen (LH2) storage, since currently no efficient cryocoolers exist that operate at very low LH2 temperatures (∼20K). Even small heat leaks under microgravity conditions and over the period of many months give rise to a complex slowly-developing, large-scale spatiotemporal physical phenomena in a multi-phase liquid-vapor mixture. These phenomena are not well-understood nor can be easily controlled. They can be of a potentially hazardous nature for long-term on-orbital cryogenic storage, propellant loading, tank chilldown, engine restart, and other in-space cryogenic fluid management operations. To support the engineering design solutions that would mitigate these effects a detailed physics-based analysis of heat transfer, vapor bubble formation, growth, motion, coalescence and collapse is required in the presence of stirring jets of different configurations and passive cooling devices such as MLI, thermodynamic vent system, and vapor-cooled shield. To develop physics-based models and correlations reliable for microgravity conditions and long-time scales there is a need for new fundamental data to be collected from on-orbit cryogenic storage experiments. Our report discusses some of these physical phenomena and the design requirements and future studies necessary for their mitigation. Special attention is paved to the phenomena occurring near MLI penetrations.

15. SUBJECT TERMS

16. SECURITY CLASSIFICATION OF:			17. LIMITATION OF ABSTRACT	18. NUMBER OF PAGES	19a. NAME OF RESPONSIBLE PERSON
a. REPORT	b. ABSTRACT	c. THIS PAGE			STI Help Desk (email: help@sti.nasa.gov)
U	U	U	UU	46	19b. TELEPHONE NUMBER *(Include area code)* (443) 757-5802

Standard Form 298 (Rev. 8/98)
Prescribed by ANSI Std. Z39.18